CWI Syllabi

CWI
P.O. Box 94079, 1090 GB Amsterdam, The Netherlands
Telephone + 31 - 20 592 9333
Telefax + 31 - 20 592 4199
WWW page http://www.cwi.nl/publications_bibl/

CWI is the nationally funded Dutch institute for research in Mathematics and Computer Science.

Proceedings of the Thirty-third European Study Group with Industry

Leiden, The Netherlands, 14 -18 September 1998

1991 Mathematics Subject Classification: 00B25, 94AXX, 62NXX, 35QXX, 73XX, 78XX, 68TXX
ISBN 90 6196 486 5
NUGI-code: 811

33rd European Study Group with Industry
14 – 18 September 1998

Wiskunde Toegepast – Mathematics Applied

To those who look at the world in the right way mathematics is everywhere: the sun comes up, a river meanders and takes along grains of sand, an airplane soars into the sky. All these events can be brought down to mathematical equations. The working of equipment in a factory or even seemingly accidental happenings, predictions of the stock market, the weather or traffic jams, nothing escapes from mathematical analysis. So it almost goes without saying that mathematics is a tool to attack practical problems. It is this idea that lies behind the research program *Wiskunde Toegepast.*

The focus of *Wiskunde Toegepast* is on the support of research projects in universities, where mathematics is developed inspired by practical problems, problems of factories, of companies, of society. In these research projects mathematicians probe new ways to look at practical questions, using existing mathematics or developing new tools. The biggest challenge of work like this is to really bridge the gap between theory and practice. But at the same time, if this succeeds, it brings enormous satisfaction. Some examples of recent successes are a computer program for the calculation of airflow along propeller blades, algorithms that help in the determination of the place of an earthquake, calculation of the behaviour of light in glass fibres, improvement of the images produced by scanning microscopes.

Most of the research in Wiskunde Toegepast is done in PhD and postdoc projects, taking around four years. In a Study Group with Industry however, the challenge to cross the bridge to practice is much more explicitly present than in a four year project. The person of the problem owner is there on Monday and he or she expects some answer by Friday. Past experience shows that mathematicians working in multi disciplinary groups can create solutions that otherwise take much more time to develop. Practical implementation of the solution, generally the most difficult goal, is almost certain. It is for this reason that the Program Committee of *Wiskunde Toegepast* decided to support the Study Group with Industry in the Netherlands: we hope to see Mathematics Applied.

Marijke de Jong
secretary of the program

NOTE: *Wiskunde Toegepast* is a joint research program of the Technology Foundation STW and the Council for Physical Sciences of the Netherlands Organization for Scientific Research NWO.

33rd European Study Group with Industry
14 – 18 September 1998

Contents

P.C. Boon, H. Hendriks, C.A.J. Klaasen, R. Muijlwijk 1
To t or not to t?

H.J. Broersma, J, Hurink, N. Bruin, L.E. Meester, 13
S.S. Op de Beek
Throughput of ADSL Modems

F. van Beckum, J.B. van den Berg, S.J. Chapman, P.W. Hemker, 29
J. Jansen, R. Mattheij, T. Myers, M. Peletier,
F. Quiros, K. Verhoeven
Laser Drilling

T. Myers, S. Rienstra et al. 39
Thermally Pressing Corner profiles

J. Schreuder, B. van de Fliert, J. Molenaar 55
Detection of Metastases in Human Lungs from CT-Scans

C.J. van Duijn, J. Hulshof, R. van der Hout, J.H. Smink 63
Stability of Stationary Velocity Profiles in Fiber Spinning

33rd European Study Group with Industry
14 – 18 September 1998

pp. 1 – 10

To t or not to t?

Pieta C. Boon
Faculty of Mathematical Sciences, University of Twente
P.O. Box 217, 7500 AE Enschede, The Netherlands
e-mail: p.c.boon@math.utwente.nl

Harrie Hendriks
Department of Mathematics, University of Nijmegen
P.O. Box 9010, 6500 GL Nijmegen, The Netherlands
e-mail: hhendr@sci.kun.nl

Chris A.J. Klaassen [1]
Korteweg - de Vries Institute for Mathematics
Institute for Business and Industrial Statistics (IBIS UvA BV), University of Amsterdam
Plantage Muidergracht 24, 1018 TV Amsterdam, The Netherlands
e-mail: chrisk@wins.uva.nl

Rolf Muijlwijk
NMi Van Swinden Laboratorium BV
P.O. Box 654, 2600 AR Delft, The Netherlands
e-mail: rmuijlwijk@nmi.nl

Consider an unknown distribution with a symmetric unimodal density and the induced location-scale family. We study confidence intervals for the location parameter based on Student's t-statistic, and we conjecture that the uniform distribution is least favorable in that it leads to confidence intervals that are largest given their coverage probability. This conjecture is supported by an argument based on second order asymptotics in the sample size and on asymptotics in the length of the confidence interval, and by simulation results. Consequently, our answer to the question in the title of this paper is: "Yes, provided the t-statistic confidence interval is based on the assumption of uniformity of the random variables generating the observations."

1. Student's t-statistic

Consider a location-scale family of distributions with the mean as location and the standard deviation as scale parameter. We are interested in confidence intervals for the location parameter based on observations that will be viewed as

[1] Corresponding author

realisations of independent and identically distributed (i.i.d.) random variables from this location-scale family. We will adopt the following notation.

Let $X_1, \ldots, X_n$ be i.i.d. random variables with distribution function

$$P(X_i \leq x) = F_{\mu,\sigma}(x) = F(\frac{x-\mu}{\sigma}),\ x \in \mathbb{R},\ i = 1, \ldots, n. \tag{1.1}$$

Here μ is the unknown location parameter and σ denotes the unknown scale parameter. The distribution function $F = F_{0,1}$ is standardized such that

$$E_F X_1 = 0, \quad \mathrm{var}_F X_1 = E_F X_1^2 = 1, \tag{1.2}$$

i.e. the standard distribution function F has mean 0 and variance 1. Consequently, we have

$$E_{F_{\mu,\sigma}} X_1 = \mu,\ \mathrm{var}_{F_{\mu,\sigma}} X_1 = \sigma^2. \tag{1.3}$$

The realizations $x_1, \ldots, x_n$ of $X_1, \ldots, X_n$ are called observations. A confidence interval for μ is an interval $I(x_1, \ldots, x_n)$ based on the observations, to which the following statement is attached: the value of the location parameter is contained in the interval, i.e.

$$\mu \in I(x_1, \ldots, x_n).$$

This statement may be true or false. The stochastic version of this statement has confidence level $1 - \alpha$, if for all $\mu \in \mathbb{R},\ \sigma > 0$, we have

$$P_{F_{\mu,\sigma}}(\mu \in I(X_1, \ldots, X_n)) \geq 1 - \alpha. \tag{1.4}$$

One also phrases (1.4) as "the coverage probability equals at least $1 - \alpha$."

We will denote the sample mean $n^{-1}\Sigma_{i=1}^n X_i$ by $\bar{X}_n$ and the sample variance $(n-1)^{-1}\Sigma_{i=1}^n (X_i - \bar{X}_n)^2$ by S_n^2 with $S_n \geq 0$. Note that the statistic

$$T_n(\mu) = \frac{\sqrt{n}(\bar{X}_n - \mu)}{S_n} \tag{1.5}$$

is location and scale invariant, i.e. its distribution under $F_{\mu,\sigma}$ is the same as the distribution of $T_n = T_n(0) = \sqrt{n}\bar{X}_n/S_n$ under F. It is called Student's t-statistic. If F equals the standard normal distribution function Φ, then under $\Phi_{\mu,\sigma}(\cdot) = \Phi((\cdot - \mu)/\sigma)$ the t-statistic $T_n(\mu)$ has a Student t-distribution with $n-1$ degrees of freedom. This distribution is called after Student, pseudonym of William Sealy Gosset, who was chemist and Brewer-in-Charge of the Experimental Brewery of Guinness' Brewery. Gosset determined the density of the t-statistic from (1.5) under normality as a function of $t \in \mathbb{R}$ as

$$\frac{\Gamma(n/2)}{\sqrt{\pi(n-1)}\,\Gamma((n-1)/2)} \left(1 + \frac{t^2}{n-1}\right)^{-n/2} \tag{1.6}$$

in Section III of his paper Student (1908).

Let $t_{n-1}(p)$ denote the p-th quantile of Student's t-distribution with $n-1$ degrees of freedom, i.e.

$$P_\Phi(T_n \leq t_{n-1}(p)) = p,\ 0 < p < 1. \tag{1.7}$$

Via the equivalence

$$T_n \leq t \Leftrightarrow \mu \geq \bar{X}_n - t\frac{S_n}{\sqrt{n}}$$

we obtain

$$I_\alpha = \left[\bar{X}_n - t_{n-1}(1-\tfrac{1}{2}\alpha)\tfrac{S_n}{\sqrt{n}},\ \bar{X}_n - t_{n-1}(\tfrac{1}{2}\alpha)\tfrac{S_n}{\sqrt{n}}\right]. \tag{1.8}$$

as a confidence interval, based on the t-statistic, for the location parameter μ with coverage probability $1-\alpha$, provided the underlying distribution of the random variables generating the observations is normal. Since T_n inherits the symmetry of the underlying distribution Φ we have $t_{n-1}(\frac{1}{2}\alpha) = t_{n-1}$ $(1-\frac{1}{2}\alpha)$ resulting in the interval

$$I_t(X_1,\ldots,X_n) = [\bar{X}_n - t\tfrac{S_n}{\sqrt{n}},\ \bar{X}_n + t\tfrac{S_n}{\sqrt{n}}] \tag{1.9}$$

with $t = t_{n-1}(1-\frac{1}{2}\alpha)$. Note that this interval is symmetric around $\bar{X}_n$.

In daily practice, this confidence interval is used extremely frequently. It is the classical, standard method for constructing confidence intervals for location parameters. The NMi Van Swinden Laboratorium (Nederlands Meetinstituut) also uses it routinely, since it is agreed upon as an international standard. However, quite often the observations may not be viewed as stemming from normal random variables and consequently, one is not sure then about the true coverage probability

$$P_{F_{\mu,\sigma}}\left(\mu \in I_t(X_1,\ldots,X_n)\right) = P_F\left(0 \in I_t(X_1,\ldots,X_n)\right) \tag{1.10}$$

and one is not even sure if $1-\alpha$ is still a valid confidence level, cf. (1.4). This possible non-normality of the underlying random variables has been noticed also in the practice of the NMi Van Swinden Laboratorium. To the 33rd European Study Group with Industry, Leiden, September 14–18, 1998, a naturally related question was suggested: "How should t be chosen such that the interval $I_t(X_1,\ldots,X_n)$ has confidence level $1-\alpha$ under F". This question is paraphrased by the title of this paper after Shakespeare (1601). We will discuss this question under the simplifying assumption that F be symmetric, i.e. $F(-x) = 1-F(x)$, and under the complicating assumption that the sample size n be small. In practice, sample sizes as small as 3 are not rare. Nevertheless, we will study asymptotics, as $n \to \infty$, first.

2. Asymptotics

By the Central Limit Theorem the standardized sample mean converges in distribution to a standard normal random variable, i.e.

$$\sqrt{n}(\bar{X}_n - \mu)/\sigma \xrightarrow{\mathcal{D}} \mathcal{N}(0,1) \tag{2.1}$$

as $n \to \infty$. By the Law of Large Numbers the sample variance converges in probability to σ^2, namely

$$S_n^2 = \tfrac{1}{n-1}\sum_{i=1}^{n}(X_i-\mu)^2 - \tfrac{n}{n-1}(\bar{X}_n-\mu)^2 \xrightarrow{P} \sigma^2. \tag{2.2}$$

Combining (2.1) and (2.2) we arrive at

$$T_n \xrightarrow{\mathcal{D}} \mathcal{N}(0,1) \tag{2.3}$$

as $n \to \infty$, whatever the underlying distribution function F (with finite variance). In particular, by the choice $F = \Phi$ this implies that the t-distribution converges to the standard normal distribution as the degrees of freedom converge to infinity.

The asymptotic normality (2.3) means that asymptotically the coverage probability of $I_t(X_1,\ldots,X_n)$ equals $\Phi(t) - \Phi(-t)$, or

$$\lim_{n\to\infty} P_{F_{\mu,\sigma}}\,(\mu \in I_t(X_1,\ldots,X_n)) = 2\Phi(t) - 1,\ \mu \in \mathbb{R},\ \sigma > 0,\ t > 0, \tag{2.4}$$

irrespectively of the underlying distribution function F with finite variance. Although this result implies that a confidence interval with approximate confidence level $1-\alpha$ may be constructed by choosing $t = \Phi^{-1}(1-\alpha/2)$ in $I_t(X_1,\ldots,X_n)$, the confidence level might be quite misleading for finite sample sizes n. A better approximate confidence interval might be obtained by application of Edgeworth expansions for the distribution function of T_n. In fact, this yields the following approximation, with φ denoting the standard normal density.

THEOREM 2.1 *Let F be symmetric and non-singular. If F has finite fourth moment, then $\kappa(F) = E_F X^4 (E_F X^2)^{-2} - 3$, the deviation from normal kurtosis, is well defined and*

$$\begin{aligned} & P_{F_{\mu,\sigma}}(\mu \in I_t(X_1,\ldots,X_n)) = 2\Phi(t) - 1 \\ + \ & \tfrac{t}{6n}\{\kappa(F)(t^2-3) - 3t^2 - 3\}\varphi(t) + o(\tfrac{1}{n}) \end{aligned} \tag{2.5}$$

holds uniformly in t. In other words, if the t-statistic confidence interval $I_t(X_1,\ldots,X_n)$ has coverage probability

$$P_{F_{\mu,\sigma}}(\mu \in I_t(X_1,\ldots,X_n)) = 1-\alpha,\ \mu \in \mathbb{R},\ \sigma > 0, \tag{2.6}$$

under F, then

$$\begin{aligned} t = \Phi^{-1}(1-\tfrac{\alpha}{2})\{1 + \tfrac{1}{12n}[-\kappa(F)(\{\Phi^{-1}(1-\tfrac{\alpha}{2})\}^2 - 3) \\ +3\{\Phi^{-1}(1-\tfrac{\alpha}{2})\}^2 + 3]\} + o(\tfrac{1}{n}). \end{aligned} \tag{2.7}$$

PROOF Straightforward application of the Theorem of Hall (1987) yields (2.5). Note that Hall's T_0 equals $\sqrt{1+1/(n-1)}\,T_n$ and hence his y has to be replaced by $t + (2n)^{-1}t$. Since this expansion (2.5) is uniform in t the second statement is implied by it. □

Let us assume

$$\alpha < 2(1 - \Phi(\sqrt{3})) = 0.0832. \tag{2.8}$$

Then, the right-hand side of (2.7) is decreasing in $\kappa(F)$. Consequently, the confidence interval $I_t(X_1, \ldots, X_n)$ has coverage probability at least $1 - \alpha$ for all F if t satisfies (2.7) with $\kappa(F)$ minimal. Under all distributions F, the deviation from normal kurtosis $\kappa(F)$ equals at least -2, i.e.

$$\kappa(F) = E_F X^4 (E_F X^2)^{-2} - 3 \geq -2, \tag{2.9}$$

in view of $(E_F X^2)^2 \leq E_F X^4$. Equality is attained in (2.9) if X^2 is degenerate. However, in many applications this is not a natural distribution. Moreover, if n is small, $n < 1 - \log \alpha / \log 2$, then a bounded confidence interval for μ based on Student's t-statistic does not exist for this distribution. In fact, if $P(X = 1) = P(X = -1) = 1/2$ holds, then $P(T_n = \infty) = P(X_1 = \cdots = X_n) = 2^{1-n} > \alpha$.

In the next Section we will restrict attention to distributions F with unimodal density and we will determine the (distribution with) minimal value of $\kappa(F)$ within this class of unimodal distributions.

3. As $n \to \infty$, the uniform distribution is least favorable

Our discussion will be based on the following inequality.

THEOREM 3.1 *Let F be a distribution with a symmetric unimodal density. If F has finite fourth moment, then the kurtosis of F equals at least $9/5$, which implies*

$$\kappa(F) \geq -6/5 \tag{3.1}$$

with equality iff F is uniform.

PROOF Let f be the symmetric unimodal density of F. Then f may be written as a mixture of symmetric uniform densities. This means that there exists a probability distribution G on $(0, \infty)$ such that

$$f(x) = \int_0^\infty \tfrac{1}{2y} \mathbf{1}_{(-y,y)}(x) dG(y) \tag{3.2}$$

holds. By this representation of f we obtain for $k = 1$ or 2

$$\begin{aligned} E_F X^{2k} &= 2 \int_0^\infty x^{2k} \int_0^\infty \tfrac{1}{2y} \mathbf{1}_{(-y,y)}(x) dG(y) dx \\ &= \int_0^\infty \int_0^y \tfrac{1}{y} x^{2k} dx dG(y) = \tfrac{1}{2k+1} E_G Y^{2k}, \end{aligned} \tag{3.3}$$

and hence

$$E_F X^4 (E_F X^2)^{-2} = \tfrac{9}{5} E_G Y^4 (E_G Y^2)^{-2} \geq \tfrac{9}{5} \tag{3.4}$$

by Cauchy-Schwarz as in (2.9). Note that equality holds iff Y^2 is degenerate, i.e. iff X is uniformly distributed. □

Together with (2.7) inequality (3.1) shows that asymptotically to second order, the uniform distribution is least favorable in the class of symmetric unimodal distributions for constructing confidence intervals based on Student's t-statistic. In other words, at fixed n and $\alpha < 0.0832$ such a confidence interval is largest if the underlying distribution is uniform.
At first sight, this might seem surprising since e.g. the normal distribution itself has heavier tails than the uniform distribution. However, (2.7) seems to imply that in some sense, heavier tails in the underlying distribution of the observations result in less heavy tails for the distribution of the t-statistic and vice versa. In fact, (2.7) itself is an asymptotic version of this conjecture. For finite sample size, the situation that interests us most, this conjectured phenomenon has been formulated precisely and proved for $t \to \infty$ by Van Zwet (1964a,b). We will prove in the next section that the uniform distribution is least favorable under the unimodal distributions in that sense too.

4. As $t \to \infty$, the uniform distribution is least favorable

In this section the relative tailbehavior of $P_F(0 \notin I_t(X_1, \ldots, X_n))$ with respect to $P_H(0 \notin I_t(X_1, \ldots, X_n))$ as $t \to \infty$, will be discussed for H being the uniform distribution function.

THEOREM 4.1 *Let F and H be unimodal distributions symmetric about 0. If H is uniform, then*

$$\lim_{t\to\infty} \frac{P_F(0 \notin I_t(X_1, \ldots, X_n))}{P_H(0 \notin I_t(X_1, \ldots, X_n))} \leq 1 \tag{4.1}$$

holds.

PROOF By symmetry, the left-hand side of (4.1) equals

$$\lim_{t\to\infty} \frac{P_F(T_n \geq t)}{P_H(T_n \geq t)} = \frac{R_n(F)}{R_n(H)} = 2^n n \int_0^\infty x^{n-1} f^n(x) dx \tag{4.2}$$

with

$$R_n(F) = \lim_{t\to\infty} \frac{P_F(T_n \geq t)}{P_\Phi(T_n \geq t)} \tag{4.3}$$

introduced and studied by Hotelling (1961); cf. his (3.2) and (3.6). According to Theorem 6.2.1 of Van Zwet (1964a) $R_n(H) \geq R_n(F)$ holds for F and H symmetric about 0, if $F^{-1}(H(x))$ is convex in $x \in (0, \infty)$. This proves the theorem, since for H uniform, this convexity of $F^{-1}(H)$ is equivalent to convexity of $F^{-1}(u)$ in $u \in (\frac{1}{2}, 1)$ which in turn is equivalent to unimodality of f.

An alternative proof may be based on (4.2) and the representation (3.2). Indeed, we have

$$\begin{aligned} \int_0^\infty x^{n-1} f^n(x) dx &= \int_0^\infty x^{n-1} \left\{ \int_0^\infty \tfrac{1}{2y} \mathbf{1}_{(0,y)}(x) dG(y) \right\}^n dx \\ \leq \int_0^\infty \int_0^\infty x^{n-1} (2y)^{-n} \mathbf{1}_{(0,y)}(x) dx dG(y) &= 2^{-n} n^{-1}. \end{aligned} \tag{4.4}$$

□

Consequently, studying the limit behavior of the coverage probability of the Student t-interval $I_t(X_1, \ldots, X_n)$ as $t \to \infty$ with n fixed, we have seen that within the class of symmetric unimodal distributions the uniform is least favorable since its confidence is converging to 1 at the smallest possible speed. The asymptotics both as $n \to \infty$ for t fixed and as $t \to \infty$ for n fixed, support the claim that the uniform distribution is least favorable. The next section adds some numerical evidence to this claim.

5. Simulation results

Fix the sample size n and the underlying distribution function F of the observations $X_1, \ldots, X_n$. Simulate $X_1, \ldots, X_n$ and compute the t-statistic. This results in the simulation Y of T_n under F. Choose N big and simulate in the same way the i.i.d. replicates $Y_1, \ldots, Y_N$ of T_n under F. We denote the order statistics by $Y_{(i)}$ with $Y_{(1)} \leq \cdots \leq Y_{(N)}$. The empirical quantile $Y_{(\lceil pN \rceil)}$ is an appropriate estimator of the p-quantile of the distribution of T_n under F.

The accuracy of this estimator may be estimated too, as described e.g. in the contribution of J.E. Walsh in Sarhan and Greenberg (1962). Let $U_{(1)} \leq \cdots \leq U_{(N)}$ be the order statistics of N i.i.d. uniform $(0, 1)$ random variables. Fix $0 < \beta < 1$ and determine the maximum value of r such that $P(U_{(r)} > p) \leq \frac{1}{2}\beta$ and the minimum value of s such that $P(U_{(s)} < p) \leq \frac{1}{2}\beta$, using the beta-distribution of the order statistics of a uniform sample. Since $F(Y_{(j)})$ and $U_{(j)}$ have the same distribution, $[Y_{(r)}, Y_{(s)}]$ is a $(1 - \beta)$-confidence interval for the p-quantile of the distribution of T_n under F. In our simulations we have used $N = 10^8$ and $p = 0.9$, 0.95, and 0.975, i.e. $\alpha = 0.2$, 0.1, and 0.05. We exploited the symmetry of the distribution by actually determining the p-th quantiles with $p = 0.8$, 0.9 and 0.95 using the absolute values $|Y_j|$. The results for a given value of n are tabulated in the row indicated by $\mathrm{df} = n - 1$.

Furthermore, we have chosen $\beta = 2(1 - \Phi(1)) \approx 0.32$ and in our simulation results below we have reported half the length $(Y_{(s)} - Y_{(r)})/2$ of the $\Phi(1) - \Phi(-1) \approx 0.68$-confidence interval $[Y_{(r)}, Y_{(s)}]$ as the value between brackets. We used this convention in analogy with the usual way of reporting a sample mean together with the standard error. The interpretation of the given value between brackets as a standard error is justified also by the fact that the point estimates $Y_{(\lceil pN \rceil)}$ are approximately in the middle of these confidence intervals as well as in the 95% confidence intervals constructed in the same way. Moreover, the 95% confidence intervals are approximately 1.96 times wider than the $(\Phi(1) - \Phi(-1))$-confidence intervals.

We have estimated the different quantiles of the same Student-t distribution via the same Monte Carlo sample of size N. Therefore the estimators in the rows of the following tables are dependent, whereas there should be no dependence between the rows.

These results show that the third digit in our simulated quantiles is very reliable. The unimodal distributions used in these simulations, are ordered

according to $\kappa(F)$ as follows

uniform	$-6/5$
triangular	$-3/5$
normal	0
Laplace	3
Cauchy	∞

(5.1)

Indeed, these results support our claim that the uniform distribution is least favorable in the class of unimodal distributions and that heavier tails (in terms of $\kappa(F)$) result in smaller quantiles for the t-statistic.

TABLE 1. Uniform distribution, estimated p-th quantiles of the t-statistic.

	p=0.9	p=0.95	p=0.975
df= 1;	3.9998(.0010)	9.0009(.0030)	18.9982(.0085)
df= 2;	2.0731(.0004)	3.5881(.0008)	5.7400(.0016)
df= 3;	1.6707(.0003)	2.6314(.0005)	3.8531(.0009)
df= 4;	1.5199(.0002)	2.2577(.0004)	3.1465(.0006)
df= 5;	1.4554(.0002)	2.0737(.0003)	2.7913(.0005)
df=10;	1.3572(.0002)	1.8177(.0002)	2.2724(.0003)
df=20;	1.3171(.0002)	1.7244(.0002)	2.1002(.0003)

Straightforward computation shows that for $n = 2$ and $p \geq 3/4$ we have

$$t_{n-1}(p) = t_1(p) = \tfrac{1}{2}(1-p)^{-1} - 1 \tag{5.2}$$

under the uniform distribution, yielding in Table 1 the exact values 4, 9 and 19, respectively, for df=1. An analytic calculation as in Perlo (1933) shows that the exact values for df=2 are 2.073664, 3.589439 and 5.741739.

TABLE 2. Triangular distribution, estimated p-th quantiles of the t-statistic.

	p=0.9	p=0.95	p=0.975
df= 1;	3.1384(.0007)	6.5498(.0021)	13.2634(.0059)
df= 2;	1.9043(.0003)	2.9574(.0006)	4.3999(.0011)
df= 3;	1.6556(.0002)	2.3911(.0004)	3.2321(.0006)
df= 4;	1.5420(.0002)	2.1670(.0003)	2.8331(.0005)
df= 5;	1.4780(.0002)	2.0409(.0003)	2.6217(.0004)
df=10;	1.3678(.0002)	1.8183(.0002)	2.2492(.0003)
df=20;	1.3218(.0002)	1.7252(.0002)	2.0932(.0002)

TABLE 3. Laplace (double exponential) distribution, estimated p-th quantiles of the t-statistic.

	p=0.9	p=0.95	p=0.975
df= 1;	2.5011(.0005)	5.0027(.0016)	10.0066(.0045)
df= 2;	1.7299(.0002)	2.4583(.0004)	3.4764(.0008)
df= 3;	1.5834(.0002)	2.1321(.0003)	2.7317(.0005)
df= 4;	1.5135(.0002)	1.9981(.0003)	2.4902(.0004)
df= 5;	1.4717(.0002)	1.9248(.0002)	2.3657(.0003)
df=10;	1.3847(.0002)	1.7861(.0002)	2.1490(.0003)
df=20;	1.3371(.0002)	1.7180(.0002)	2.0529(.0002)

In Table II on page 337 of Hotelling (1961) $t_2(0.975)$ has been computed as 3.48, in accordance with our simulations.

TABLE 4. Cauchy distribution, estimated p-th quantiles of the t-statistic.

	p=0.9	p=0.95	p=0.975
df= 1;	2.0825(.0004)	4.0779(.0012)	8.1157(.0036)
df= 2;	1.5342(.0002)	2.1265(.0003)	2.9412(.0007)
df= 3;	1.4241(.0002)	1.8558(.0002)	2.3551(.0004)
df= 4;	1.3769(.0002)	1.7485(.0002)	2.1475(.0003)
df= 5;	1.3506(.0001)	1.6908(.0002)	2.0417(.0003)
df=10;	1.3018(.0001)	1.5881(.0002)	1.8618(.0002)
df=20;	1.2793(.0001)	1.5422(.0002)	1.7849(.0002)

Hotelling (1961) derived $t_2(p)$ for the Cauchy distribution as (cf. his (6.41))

$$t_2(p) = (1 - 3\mathrm{tg}^2(\pi(2p-1)/6))^{-1/2},\ p \geq \tfrac{1}{2} + \tfrac{3}{\pi}\,\mathrm{arctg}\tfrac{1}{2}, \tag{5.3}$$

which leads to $t_2(0.975) = 2.9412$ in line with our results (note that $t_2(0.995) = 6.46$ and not 3.69 as in (6.42) and Table II of Hotelling (1961)).

For the sake of validation of the method we also compiled the next table, which might be compared to the last one.

TABLE 5. Normal distribution, estimated p-th quantiles of the t-statistic.

	p=0.9	p=0.95	p=0.975
df= 1;	3.0767(.0007)	6.3098(.0020)	12.7031(.0054)
df= 2;	1.8857(.0003)	2.9202(.0006)	4.3023(.0011)
df= 3;	1.6378(.0002)	2.3530(.0004)	3.1819(.0006)
df= 4;	1.5334(.0002)	2.1319(.0003)	2.7764(.0005)
df= 5;	1.4757(.0002)	2.0151(.0003)	2.5707(.0004)
df=10;	1.3721(.0002)	1.8125(.0002)	2.2281(.0003)
df=20;	1.3253(.0002)	1.7246(.0002)	2.0857(.0003)

TABLE 6. Normal distribution, exact p-th quantiles of the Student t-statistic.

	p=0.9	p=0.95	p=0.975
df= 1:	3.077684	6.313752	12.7062
df= 2:	1.885618	2.919986	4.302653
df= 3:	1.637744	2.353363	3.182446
df= 4:	1.533206	2.131847	2.776445
df= 5:	1.475884	2.015048	2.570582
df=10:	1.372184	1.812461	2.228139
df=20:	1.325341	1.724718	2.085963
df=∞:	1.281552	1.644854	1.959964

6. Conclusion

Consider the location problem with an unknown symmetric distribution. Confidence intervals for the location parameter may be based on Student's t-statistic. If the underlying distribution of the observations is known to have a unimodal density this can be done in a conservative way by assuming uniformity of the underlying distribution, if (2.8) holds. In other words, if the t-value in (1.9) is chosen according to the third column of Table 1 then the coverage probability will be at least $2p - 1 = 1 - \alpha = 0.95$, *whatever the unknown symmetric unimodal distribution of the observations.* This claim is supported by the Edgeworth expansion of Section 2 and its consequence of Section 3, by the finite sample analysis of the far tails in Section 4, and by the Monte Carlo results of Section 5.

Standard approaches like the bootstrap (i.e. estimating F) and empirical Edgeworth expansion (i.e. estimating $\kappa(F)$ in (2.5)) are based completely on asymptotic considerations as $n \to \infty$. Consequently, for small sample sizes these techniques are not reliable whereas for large sample sizes the gain in efficiency as compared to our recommendation of using the uniformity assumption, is not dramatic; compare Tables 1 and 6 and note that for $n = 21$ the relative difference in interval length is less than 0.7%.

Acknowledgement We would like to thank the referee for useful suggestions, especially for the reference to Van Zwet (1964a), which led to our Theorem 4.1.

References

1. Bowman, K.O., Beauchamp, J.J. and Shenton, L.R. (1977). The distribution of the t-statistic under non-normality. *Internat. Statist. Rev.* **45**, 233–242.
2. Hall, P. (1987). Edgeworth expansion for Student's t statistic under minimal moment conditions. *Ann. Probab.* **15**, 920–931.
3. Hotelling, H. (1961). The behavior of some standard statistical tests under nonstandard conditions. *Proc. Fourth Berkeley Symp. Math. Statist. Probab.* (Neyman, J. (ed.)) **I**, 319–359.
4. Perlo, V. (1933). On the distribution of Student's ratio for samples drawn from a rectangular distribution. *Biometrika* **25**, 203-204.
5. Sarhan, A.E. and Greenberg B.G. (1962). *Contributions to order statistics.* Wiley, New York.
6. Shakespeare, W. (1601). *Hamlet, Prince of Denmark,* Act III, Scene i, line 56.
7. Student (1908). The probable error of a mean. *Biometrika* **6**, 1–25.
8. Van Zwet, W.R. (1964a). *Convex Transformations of Random Variables,* Mathematical Centre Tracts 7, Mathematical Centre, Amsterdam.
9. Van Zwet, W.R. (1964b). Convex transformations: A new approach to skewness and kurtosis. *Statist. Neerlandica* **18**, 433–441.

33rd European Study Group with Industry
14 – 18 September 1998

pp. 11 – 26

Throughput of ADSL Modems

H.J. Broersma, J. Hurink
Universiteit Twente, Fac. Toegepaste Wiskunde,
Postbus 217, 7500 AE Enschede

N. Bruin
Rijksuniversiteit Leiden, Vakgroep SSOR,
Mekelweg 4, 2628 CD Delft

L.E. Meester
Technische Universiteit Delft

S.S. Op de Beek
KPN-Research

J. Westhuis
MARIN

This paper considers the throughput of ADSL (Asymmetric Digital Subscriber Line) modems, used for high speed data transmission over relatively unreliable connections, e.g., copper telephone wires. The modem technique uses an error correcting code and interleaving. The settings include a grouping factor S which affects the amount of data per code word, the number of redundant bytes per code word (R) and the interleave depth D. The influence of these parameters on both the effective data transmission rate and the resulting error rate in the received signal are determined for two error situations: random errors and bursts of errors. An approximate analysis for the random error case of the throughput of a TCP (Transport Control Protocol) connection using an ADSL modem shows that maximum throughput is obtained for the highest values of S and R.

1. Introduction

In providing data services, such as Internet access to customers, the voice band modems or even ISDN modems with maximum bit rates of 56 kbit/s and 64 kbit/s, respectively, form a bottle neck in the transmission. The recently standardised Asymmetric Digital Subscriber Line or ADSL modems [1] form a breakthrough in the access data rate by offering rates of several Mbit/s through the copper telephony infrastructure. High bit rate services, such as Video on Demand, Video conferencing or fast Internet can now be offered to and from a customer location. All these services have in common that the downstream

data rate is much larger than in the upstream direction, which is reflected in the Asymmetric Digital Subscriber Line described below.

In this paper we examine the performance of TCP, the widely used Transport Control Protocol in the Internet, in case transmission is provided by an ADSL modem. In Section 1.2 the essential properties of TCP are described. Its performance is assessed by the TCP throughput: the net amount of correctly transmitted data per unit of time. TCP throughput in the Internet has been a subject of study for many years; its steady state performance has been analysed in [2, 3, 4]. The special case we study in this paper concerns the throughput of TCP over an ADSL link. Essentially, three specific ADSL aspects are of importance in this study:

1. the raw bit rate of the ADSL link,
2. the error correction techniques used in ADSL, and
3. the asymmetry of the data link.

The last issue will not be treated in this paper. Extensive study of the influence of the asymmetry of a data link on TCP throughput is described in [5]. The application of error correction techniques is inevitable in an ADSL modem, in order to obtain a reliable transmission link. The effective number of transmission errors in the ADSL data link depends on the adjustable settings in the data encoder. Section 2 treats the influence of the coding and the adjustable parameters, leading to an analysis whether and how transmission errors propagate to the decoded data stream. The influence of the remaining data transmission errors on the TCP throughput is described in Section 3. Finally, numerical results of the TCP throughput as a function of some typical ADSL settings are presented in Section 4.

1.1. ADSL

The Asymmetric Digital Subscriber Line (ADSL) is a modem technique that uses the copper telephony infrastructure to offer broadband data connections from a central office to subscribers. The asymmetry is due to the fact that generally, in high bandwidth applications, the data stream from the central office to the users is larger than the data stream in the opposite direction. By taking advantage of the asymmetry of the service, a higher downstream bandwidth can be achieved than with symmetrical modem techniques. The maximum raw bit rate typically is 8 Mbit/s from the Central Office (CO) to the customer (downstream direction), and 1 Mbit/s from the customer to the CO (upstream direction). The actual achieved bit rates strongly depend on the distance bridged by the modem pair and noise induced by other systems.

There are two different causes for bit errors in the local loop and for each of these ADSL takes different protective measures. The first cause of bit errors is the noise induced by other systems combined with the length of the copper cable. ADSL deals with this problem at start-up: it evaluates the line characteristics and estimates the induced noise on the transmission line. The initial transmission rate is optimised for the length and noise found. According to the

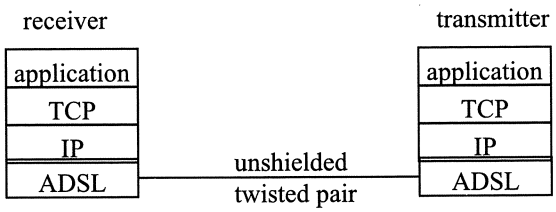

FIGURE 1. Typical protocol stack used in ADSL modems

ANSI ADSL standard [1], the maximum bit rate is determined such that the bit error ratio (BER) is less then 10^{-7}.

The second cause for bit errors is impulse noise. A common cause for impulse noise is the on and off switching of electrical equipment. This results in a short, but very strong disturbance of the line. Impulse noise can last from microseconds to several tens of milliseconds and results in a burst of bit errors. An interleaving technique increases the robustness of the ADSL modem for bit error bursts. Interleaving introduces an additional delay, typically between 10 and 60 milliseconds.

A typical protocol stack used in ADSL is shown in Figure 1.

1.2. TCP

The Transmission Control Protocol (TCP) provides a highly reliable stream of packets between transport layers on internet hosts by requiring acknowledgements from the receiving transport layer within a specified period of time. Furthermore, by providing sequence numbers, packets can be delivered in the order that they were sent. Error checking of each packet is provided by a check sum transmitted as part of the TCP header. TCP makes no assumption as to the reliability of the lower-level protocol. To achieve this level of control and reliability, a connection from the transport layer on one host to the other host must be set up before data can be transferred. Special handshake messages are defined in TCP for establishing and releasing a connection. In this paper, we will concentrate on the consequences of the flow control mechanisms in TCP. In TCP a so-called sliding window protocol is used. It allows the sender to transmit multiple packets before it stops and waits for an acknowledgement (ACK); the time until the acknowledgement of the first packet is received is called the round trip time (RTT). This leads to faster data transfer, since the sender does not have to stop and wait for an acknowledgement each time a packet is sent. Using special window update ACK messages, the receiver can inform the sender of the offered or advertised window size which depends on the receiver buffer filling. The sender can adjust its sending window to the minimum of the advertised window and the maximum window size (which is a fixed value which depends on the implementation of TCP). The process of sending packets and receiving ACKs is visualised in Figure 2. The most com-

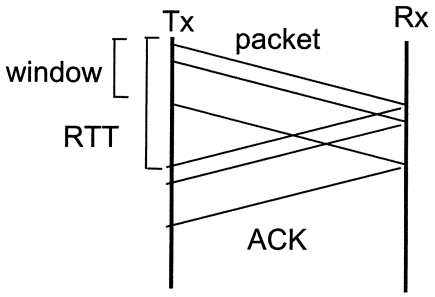

FIGURE 2. Data transfer during one Round Trip Time (RTT): a number of window packets is sent before the ACK of the first packet sent is received; Rx=receiver, Tx=sender.

mon TCP 'flavour' used in the internet today is TCP Reno. Four mechanisms are introduced in this variant in order to control the data transmission:

- Slow start. This begins by sending one packet and waiting for an acknowledgement. For each acknowledgement the sender receives, it injects two packets into the network. This leads to an exponential increase in the number of packets sent per RTT. The slow start phase ends when the receiver's advertised window is reached.
- Congestion avoidance. This mechanism is used to probe the network for available bandwidth by sending one additional packet for each RTT (up to the receivers advertised window). In the original slow start/congestion avoidance scheme, when the sending TCP detects packet loss (indicating congestion), it drops back into slow start until the packet sending rate is half the rate at which the loss was detected and then begins congestion avoidance.
- Fast retransmit and fast recovery. Fast retransmit reduces the time it takes a TCP sender to detect a single dropped packet. Rather than waiting for the retransmit timeout (RTO), the TCP sender can retransmit a packet if it receives three duplicate ACKs for the packet sent immediately before the lost packet. Fast recovery is closely related to fast retransmit: as mentioned before, when a sender retransmits a packet, it normally recovers by moving into a slow start phase followed by a congestion avoidance phase. If the sending TCP detects the packet loss using fast retransmit, however, fast recovery is used instead. Fast recovery halves the segment sending rate and begins congestion avoidance immediately, whitout falling back to slow start.

In our treatment we assume that the TCP receiver has an infinite processing capacity, i.e., the input buffer of the receiver never overflows. In Figure 3 a typical evolution of the window size as a function of time is shown for a typical TCP session. In our approach the slow start phase which is initated at connection start up, will not be taken into account.

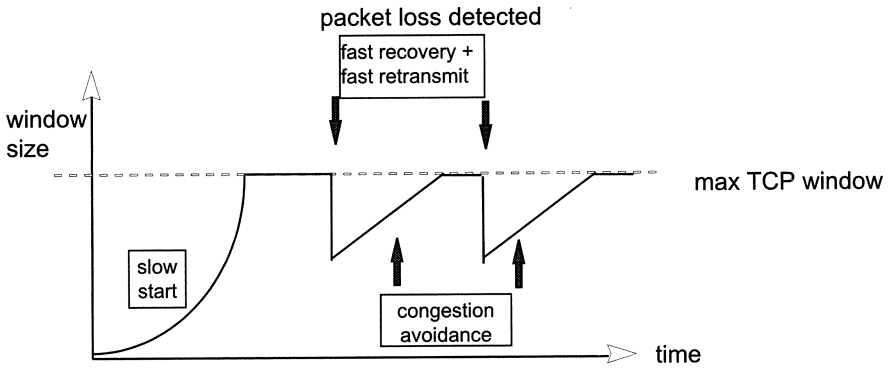

FIGURE 3. Typical behaviour of the TCP window size as a function of time

2. ADSL MODEM SPECIFICATION AND ERROR ANALYSIS

This section starts with a description of the ADSL modem in terms of its functional blocks. Not all of them are relevant to error propagation. In the error analysis that concludes this section only the relevant parts have been considered.

2.1. ADSL description

An ADSL modem can be divided into eight functional blocks (see Figure 4, modified from [1]). The first block groups bytes from a continuous byte stream (these bytes actually represent ATM cells) into a so-called multiplexer or Mux frame. This byte stream is supplied through one of two channels:

- The fast channel: data that is supplied through this channel follows a different functional path in the modem, resulting in a relatively short time delay of the byte stream. The drawback of this mode is that it has a relatively high error rate.
- The interleaved channel: this channel provides a relatively lower error rate, at the cost of a larger time delay.

The Mux-framer also adds a synchronization byte to the data in the Mux frame. Before actual transmission several Mux frames are assembled into one superframe. The second functional block computes Cyclic Redundancy Check (CRC) bits over a collection of frames that is to constitute one superframe. This check is used for internal evaluation only. The management system of the ADSL modem uses the CRC bits to keep track of the 'severely errored seconds' (SES) and 'errored seconds' (ES) statistics. The third functional block scrambles the data bytes in the framed byte stream to ensure that the resulting byte signal has a random character. In the case of the fast path, the bytes of a single Mux frame are coded directly into a so-called ADSL frame (functional block 4) using a Reed-Solomon coding algorithm. This Forward Error Correction

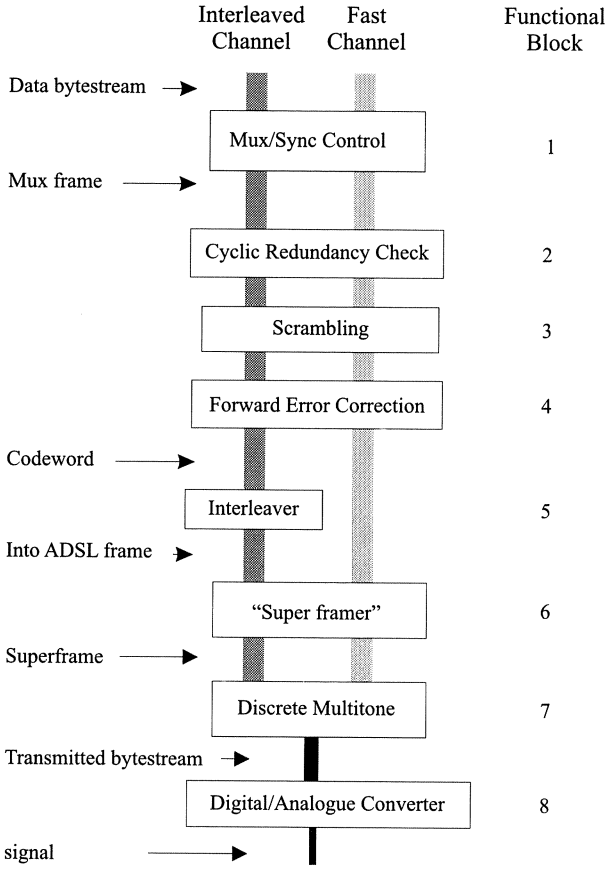

FIGURE 4. Functional blocks in an ADSL modem.

(FEC) coding ensures that when a small number of bytes in the code word is corrupted, the original Mux frame stored in the code word can still be recovered. The number of redundancy bytes per code word, added to the original signal for Forward Error Correction, can be adjusted and is denoted by R. The maximum number of error bytes that can be corrected increases as R increases (see Section 2.2).

When the interleaved buffer is used, multiple Mux frames are coded in a single code word and this code word is then interleaved with other code words from the interleaved buffer (fifth functional block). The main purpose of this is to spread the byte errors of a burst. We come back to this in Section 2.2.2. After the interleaving process, interleaved code words are partitioned into ADSL frames. The number of Mux frames per code word is denoted by S, the interleave depth is denoted by D; both these parameters can be adjusted.

In the sixth functional block, ADSL frames (which may originate from the fast or the interleaved path) are grouped, 68 at a time, into a superframe, and the originally computed CRC checksum is stored in the synchronization byte of the first ADSL frame of the superframe (functional block 7). Every ADSL frame in a superframe is modulated into a Discrete Multitone (DMT) symbol (seventh functional block). The total superframe consists of the original 68 frames plus an additional DMT symbol for synchronization purposes.

The Digital Analog Converter (last functional block) converts the stream into an electrical signal that is sent over the copper telephony infrastructure.

The question that we address is how the performance of the connection (both at ADSL and at TCP level) depends on the 'free' parameters R (number of additional FEC bytes per code word), S (number of Mux frames coded into a single code word) and D (interleave depth), considering both random and burst errors.

2.2. Error propagation at the ADSL level

First of all, we simplify the modelling by ignoring the scrambler and the conversion of the byte stream to DMT symbols and the digital-analog conversion. Furthermore, in the model we disregard the cyclic redundancy check since it is used for internal purposes only and has no influence on the behaviour or characteristics of the modem.

When the interleaved channel is used, S Mux frames are supplemented with R redundant bytes in order to create a code word. These code words are then interleaved to depth D. From a modelling point of view, we can identify the fast and the interleaved channels by assuming that the fast buffer equals the interleaved buffer with settings $S = 1$ and $D = 1$.

We shall use μ to denote the bandwidth of the physical link, in *bytes* per second; for computations we use $\mu = 2^{18} = 262144$, which corresponds to 2 Mbits/s. The baudrate, the number of superframes sent per second is nominally 4000, but because of the additional (the 69th) synchronization frame in the ADSL superframe, the actual baudrate is only $\frac{68}{69}$ of 4000. This means that it takes $\frac{68}{69} \cdot 0.25$ ms to send an ADSL frame, and so one obtains for the number of bytes in an ADSL frame:

$$N = \left\lfloor \frac{68}{69} \cdot 0.25 \cdot 10^{-3} \mu \right\rfloor \approx \lceil 2.46 \cdot 10^{-4} \mu \rceil = \alpha \mu;$$

the fixed factor α is introduced for notational convenience. The length of a code word in bytes, denoted by n, is a fundamental quantity in the analysis; it equals NS, so in fact n directly depends on the free parameter S. A code word contains information equivalent to $k = n - R$ bytes.

The fraction of actual data in an ADSL frame is determined by the number of synchronization bytes and redundant bytes from Forward Error Correction. In the case that S Mux frames are used to form a code word containing R redundant bytes, the final code word will be split into S ADSL frames, implying that the number of error correction bytes per ADSL frame equals R/S. The

number of synchronization bytes in a Mux frame varies between 1 and 3; we will denote this unknown number as h and use $h = 2$ in computations. Thus the number of data bytes in an ADSL frame is $K = N - h - R/S$.

So a priori, without any considerations about errors, the efficiency of the ADSL modem, i.e., the number of data bytes transmitted divided by the actual number of bytes sent, given the parameters R, S and μ is:

$$\eta_{\text{ADSL}} = \frac{K}{N} = 1 - \frac{h + \frac{R}{S}}{\alpha\mu}.$$

Random errors

In this case we assume that transmitted bytes are corrupted with probability p each, independently of the others. Whether interleaving is applied or not, the number of corrupted bytes has a Binomial distribution with parameters n and p. The probability that i bytes in a code word are corrupted is given by:

$$\binom{n}{i} p^i (1-p)^{n-i}.$$

The S Mux frames are encoded by an $(n, k, n-k+1)$ Reed-Solomon code over $\mathbb{F}_{256}$, which means that a data word of k bytes is coded as a code word of n bytes, such that distinct data words are coded as code words that differ in at least $n - k + 1$ bytes. This implies that the original data word can still be recovered from a code word that has at most $e = \frac{1}{2}(n-k)$ damaged bytes.

Therefore the probability q, that the Mux frames coded in a Reed-Solomon code word cannot be recovered, given a byte error probability p, is given by

$$q = \text{P(code word error)} = \sum_{i=e+1}^{n} \binom{n}{i} p^i (1-p)^{n-i}. \tag{1}$$

Random errors in the byte stream occurring with probability p result in a similar error process at code word level, but with (a smaller) probability q. An error in the code word stream, however, implies that *all* data bytes encoded into this code word are corrupted.

Bursts of errors

In the following we will analyse the effect of bursts of errors. We assume that a burst will lead to a complete corruption of L consecutive bytes in the byte stream. Furthermore, for sake of simplicity, we assume for the moment that the length L is a multiple of the interleave depth D: $L = cD$. Our aim is to get a relation between the length L of a burst and the (expected) number of lost code words (those that cannot be corrected by the Reed-Solomon code) in relation to the modem parameters. In this context, the main point of interest will be the interleaving.

As mentioned, code words are placed on the different layers of the interleaver and subsequently the bytes are read in such a way that each Dth byte belongs to

the same layer (in Figure 5 the bytes are transmitted by reading columnwise). Thus a burst of length $L = cD$ leads to c consecutive corrupted bytes in each layer (see Figure 5).

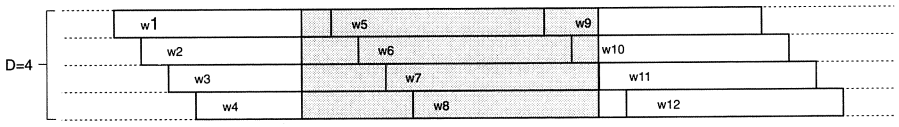

FIGURE 5. Sketch of a burst

In order to determine the number of lost code words, we consider the layers separately. Although the position of the first corrupted byte within a code word differs between the layers, the expected number of corrupted code words will be the same for each layer.

The following lemma analyses the effect of a burst for one layer of the interleaver.

LEMMA 1 *Consider a byte stream of code words of length n which are coded by a Reed-Solomon code with $R = 2e$ redundant bytes. The expected number of corrupted code words for a burst of length c is given by:*

$$E = \begin{cases} 0 & \text{if } c \leq e, \\ 1 + \frac{c-2e-1}{n} & \text{if } c \geq e+1, \end{cases}$$

PROOF: In the case $c \leq e$, each code word has at most e corrupted bytes and, thus, each code word can be corrected by the Reed-Solomon code.

To analyse the case $c \geq e+1$, consider the position t of the first byte of the burst within a code word ($t = k$ means that the first destroyed byte is the kth byte of some code word). Let cw_1 denote the code word containing the first byte of the burst and let $cw_2, cw_3, \ldots$ denote the following code words.

To determine the total number of corrupted code words in dependence of t, let $b := \lceil \frac{c-e-1}{n} \rceil$. We will show that code words $cw_2, \ldots, cw_b$ are always destroyed, the possibility of correcting cw_1 and cw_{b+1} depends on t, and that the remaining code words all can be corrected.

Obviously, code word cw_1 can not be corrected if and only if $t \in \{1, \ldots, n-e\}$.

Furthermore, code words cw_i with $i \geq 2$ can not be corrected if and only if

$$t + c - 1 \geq (i-1)n + e + 1.$$

So, since

$$(b-1)n + e + 1 \leq \frac{c-e-1+n-1}{n} n - n + e + 1 = c - 1 < t + c - 1$$

we may conclude that the code words $cw_2, \ldots, cw_b$ can not be corrected.

Since $1 \leq \frac{c-e-1}{n}n - c + e + 2 \leq bn - c + e + 2 \leq \frac{c-e-1+n-1}{n}n - c + e + 2 = n$ we may conclude that code word cw_{b+1} can not be corrected if and only if $t \in \{bn - c + e + 2, \ldots, n\}$.

Finally, since $(b+1)n + e + 1 \geq \frac{c-e-1}{n}n + n + e + 1 = c + n > c + t - 1$, code words $cw_{b+2}, cw_{b+3}, \ldots$ are all correctable.

The expected number of corrupted code words now can be obtained by considering all possible values for t. Since t is uniformly distributed on $\{1, \ldots, n\}$ we get the following expected number of corrupted code words:

$$\begin{aligned} E &= \tfrac{n-e}{n} + b - 1 + \tfrac{n-(bn-c+e+2)+1}{n} \\ &= b - 1 + \tfrac{n(2-b)+c-2e-1}{n} = 1 + \tfrac{c-2e-1}{n} \end{aligned}$$

□ From the lemma, we get for the interleaver as a whole:

THEOREM 2 *Consider an ADSL modem using interleave depth D and code words of length n coded by a Reed-Solomon code with $R = 2e$ redundant bytes. A burst of length $L = cD$ ($c \in \mathbb{N}$) will result in an expected number of*

$$E = \begin{cases} 0 & \text{if } c \leq e, \\ D(1 + \frac{c-2e-1}{n}) & \text{if } c \geq e + 1, \end{cases}$$

not correctable code words.

So the maximum length of a burst that can be tackled by an interleaver with interleave depth D and a Reed-Solomon code with $R = 2e$ redundant bytes is eD bytes.

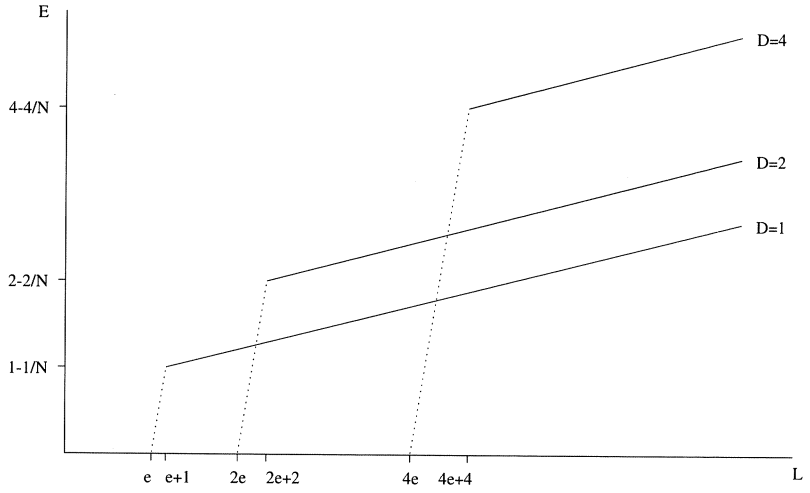

FIGURE 6. Expected number of corrupted code words for different values of D.

In Figure 6 we have sketched the expected number of corrupted code words in relation to the burst length for some values of D. It is interesting to see that

a higher interleave depth, besides the positive effect that longer burst can be handled without getting any corrupted code words, also has a negative effect: if a burst is too long to disappear completely, the expected number of corrupted code words increases with the interleave depth.

Up to now, we have focused on the expected number of corrupted code words. Of course, also the distribution is of interest, so we try to say something about the range of values that may occur. As a direct consequence of the proof of Lemma 1 we can state that a burst of length $L = cD$ leads to $b-1$, b, or $b+1$ corrupted code words per layer, where $b = \lceil \frac{c-e-1}{n} \rceil$. Furthermore, it is easy to see that this number will be equal to $b-1$ or b if $(c \mod n) \leq 2e+1$ and equal to b or $b+1$ if $(c \mod n) \geq 2e+2$. As an immediate consequence we get:

LEMMA 3 *Consider an ADSL modem using interleave depth D and code words of length n coded by a Reed-Solomon code with $R = 2e$ redundant bytes. For a burst of length $L = cD$ ($c \in \mathbb{N}$) the number F of corrupted code words belongs to the set*

$$\{mD, mD+1, \ldots, (m+1)D\} \text{ with } m = \begin{cases} b-1 & \text{if } (c \mod n) \leq 2e+1 \\ b & \text{if } (c \mod n) \geq 2e+2. \end{cases}$$

By a more detailed analysis of the dependences between the different layers of the interleaver, the possible values for F may be reduced further.

The above considerations are based on the assumption that the burst length is a multiple of the interleave depth D. However, the stated results can be adapted in a straightforward manner to general burst length $L = cD + a$ with $c \in \mathbb{N}$ and $a \in \{0, \ldots, D-1\}$ since such a burst leads to a layers with a burst of length $c+1$ and $D-a$ layers with a burst of length c.

3. EFFECT ON TCP THROUGHPUT

In this part we consider the performance of an ADSL modem link where actual data transmission is controlled by a Transport Control Protocol (TCP). We first consider the occurrence of errors as seen by TCP.

The data stream that is transformed and transmitted by the ADSL modem in fact is a stream of *packets* generated by TCP. Let g be the number of bytes in a packet. The transmitting modem chops the stream in pieces of k bytes, the data words, and, at the other end, the receiver reassembles the TCP packet stream from them. We assume that an error in a code word results in the detection of an error by TCP in any and all packets that overlap the corresponding data word. Clearly, a code word error may lead to one, two or several packet errors, depending on k, g, and whether there is any alignment. We speak of alignment when there are (periodic) instances in the byte stream where code word and packet boundaries coincide.

Now consider the loss of a randomly chosen code word. By simple counting arguments the following probabilities are easily obtained. If $k \leq g$ and there is

no alignment:

$$\text{P(one packet lost)} = 1 - \frac{k}{g}, \qquad \text{P(two packets lost)} = \frac{k}{g};$$

if there is aligment:

$$\text{P(one packet lost)} = 1 - \frac{k}{g}(1 - \frac{l}{k}), \qquad \text{P(two packets lost)} = \frac{k}{g}(1 - \frac{l}{k}),$$

where $l = \text{lcm}(k, g)$, the least common multiple of k and g.

If $k > g$ the number of lost packets is

$$\left\lceil \frac{k}{g} \right\rceil \quad \text{or} \quad \left\lceil \frac{k}{g} \right\rceil + 1.$$

If there is no alignment, it is always the latter. If there is:

$$\text{P}\Big(\left\lceil \frac{k}{g} \right\rceil \text{ packets lost}\Big) = \frac{2l}{g}, \qquad \text{P}\Big(\left\lceil \frac{k}{g} \right\rceil + 1 \text{ packets lost}\Big) = 1 - \frac{2l}{g}.$$

From these results it is concluded that random (code word) errors appear as (usually small) clusters of errors in the packet stream.

Now we consider the effect on the throughput using the Reno version of TCP in the *congestion avoidance phase*. It is convenient to consider time in a sequence of intervals of length equal to the *Round Trip Time* (RTT). TCP controls transmission by means of its adaptable *window size*, W: the amount of data to be released for transmission in the next RTT interval. The receiving TCP sends back acknowledgments for the undamaged reception of packets; damaged or lost packets are detected through the ackowledgments. In the congestion avoidance phase, if all packets sent in the previous RTT are received undamaged, the window size is increased by 1 packet; if not, the window size is halved and missing packets are retransmitted. So loss in throughput is caused largely by the reduction of the window size.

Random multiple packet loss and severe error situations result in time-outs, which cause TCP to start again with a *slow start phase* in which the window size is set to 1 packet. From the above it is clear, however, that this is an important issue, since random (single) code word errors that lead to multiple packet losses are by no means exceptional. Unfortunately, no generally valid accurate description of how TCP handles this was available, and this could not be analysed.

This also implies that the effect of error bursts on the TCP throughput can only be analysed in so far as they lead to single packet losses, though, as is clear from previous sections, this is a rare occurrence. Interleaving, however, also affects the RTT and, through the RTT, the effective throughput.

Assume that a single TCP packet is coded into a single code word (of size n) . The round trip time now consists of a fixed part, RTT_0, which consists of the time needed to do the coding and decoding and the time to send the

acknowledgement, and the time needed to actually transmit the bytes of the code word. This is roughly nD/μ seconds. So,

$$\mathrm{RTT} = \mathrm{RTT}_0 + \frac{nD}{\mu}.$$

The maximum number of bytes transmitted in one RTT is therefore

$$W_{\max} = \mu \mathrm{RTT}.$$

We assume that this maximum window size is used until an error occurs. Subsequently, $W_{\max}/2n$ error-free RTT periods are needed to re-attain the maximum window size. During this phase on average an extra $W_{\max}/4$ bytes per RTT could have been transmitted had the error not occurred. So the error results in a loss of transmission capacity of $W_{\max}^2/8n$. Assuming that each error results in a loss this size leads to an upper bound on the total loss, as the additional loss due to an error during a recovery phase is less than the loss when $W = W_{\max}$.

If q, the probability of a code word error (see also Section 2.2) is sufficiently small, then code word errors will be so infrequent that they nearly always occur when the window size is completely recovered from the previous error. Then we expect, using $W_{\max} = \mu \mathrm{RTT}$, for the effective bandwidth:

$$\mu_{\mathrm{eff}} = \mu \left(1 - q\frac{\mu^2 \mathrm{RTT}^2}{8n}\right).$$

Of course, we are interested in the number of *data* bytes we expect to transmit per second, in relation to μ. Using the result obtained in Section 2.2 for the efficiency η_{ADSL}, we obtain

$$\eta_{\mathrm{TCP}} = \frac{\mu_{\mathrm{eff}}}{\mu}\eta_{\mathrm{ADSL}} = \left(1 - \frac{q\mu^2 \mathrm{RTT}^2}{8n}\right)\left(1 - \frac{h + \frac{R}{S}}{\alpha\mu}\right). \tag{2}$$

If, for argument's sake, we assume that RTT_0 is negligible, then we can simplify this expression even further to

$$\eta_{\mathrm{TCP}} = \left(1 - \frac{1}{8}qnD^2\right)\left(1 - \frac{h + \frac{R}{S}}{\alpha\mu}\right).$$

where q depends on n and R, and n on μ and S.

	$R=0$	2	4	6	8	10	12	14	16
$S=1$	0.489	0.984	1.000	1.000	1.000	1.000	1.000	1.000	1.000
$S=2$	-0.981	0.874	0.995	1.000	1.000	1.000	1.000	1.000	1.000
$S=4$	-6.441	0.075	0.922	0.995	1.000	1.000	1.000	1.000	1.000
$S=8$	-25.4	-5.26	-0.037	0.869	0.987	0.999	1.000	1.000	1.000
$S=16$	-83.1	-35.3	-10.4	-1.8	0.44	0.905	0.986	0.998	1.000

TABLE 1. μ_{eff}/μ for $p = 0.001$, $\mu = 262144$ bytes/s, $D = 1$.

4. Results and Discussion

Using formula (2) for η_{TCP}, we can calculate the expected utilisation of the total available bandwidth during bulk data TCP-transmission over an ADSL connection with random errors occurring at some fixed rate p.

Table 1 shows the values of μ_{eff}/μ for various parameter settings. This quantity measures the throughput in relation to the throughput that would have been attained if the same settings were used over an error-free connection ($p = 0$). The negative values correspond to cases where the word error rate is so high that the assumption that word errors occur only if TCP has recovered from the previous word error, is too far from the truth.

We see that higher settings of R and lower settings of S result in an error correction that is so good that the probability of byte errors resulting in word errors is so small that their effect is smaller than the precision of the table. This table would suggest that setting R very high has no negative effect. This is misleading, as Table 2 shows. The design of ADSL modems implies that the transmission speed of data *together with* redundancy and overhead is fixed. Thus, increasing the redundancy reduces the bandwidth available to data. Note the combinations $(S, R) = (1, 2)$, $(2, 6)$ and $(4, 12)$, which have about the same η_{TCP}.

	$R=0$	2	4	6	8	10	12	14	16
$S=1$	0.474	0.923	0.907	0.877	0.846	0.815	0.785	0.754	0.723
$S=2$	*	0.834	0.933	0.923	0.908	0.892	0.877	0.862	0.846
$S=4$	*	0.0717	0.879	0.941	0.938	0.931	0.923	0.915	0.908
$S=8$	*	*	*	0.832	0.941	0.949	0.946	0.942	0.938
$S=16$	*	*	*	*	0.423	0.869	0.945	0.954	0.954

TABLE 2. η_{TCP} for $p = 0.001$, $\mu = 262144$ bytes/s, $D = 1$.

As we see, for $S = 16$, $R = 14, 16$, we have the highest value $\eta_{\mathrm{TCP}} = 0.954$. In fact, calculations to a higher precision yield that for $R = 14$, η_{TCP} is strictly larger. Thus, for the presented p and μ, $(D, S, R) = (1, 16, 14)$ gives the best expected throughput.

Since we do not consider bursts of errors in this model, interleaving will have no positive effect. On the other hand, interleaving does increase RTT and thus increases the penalty on a word error. Table 3 shows that this effect can be quite dramatic. The value for $(D, S, R) = (64, 16, 16)$ is not realistic; the RTT will be so large in this case, that the recovery periods of word errors will overlap significantly.

This discussion shows that the interleaver should only be used if we expect a significant reduction of the number of corrupted code words. Since such a reduction is only achieved if bursts can be removed completely (otherwise the use of the interleaver will even increase the number of corrupted code words slightly), the probability that a burst of length smaller than eD (see Corollary 1) occurs has to be significantly larger than 0 to get a positive effect of the use of the interleaver at depth D.

The original question was about throughput during a long transmission. That means that the penalty on large values for RTT is only felt through

the increased recovery time of the window size. In practice there is another unfortunate side-effect of large RTTs, namely a lower responsiveness of the system. For interactive applications, high responsiveness is generally highly desirable. As we saw before, assuming that packets coincide with code words,

$$\mathrm{RTT} = \mathrm{RTT}_0 + \alpha SD,$$

where $\alpha \approx 2.46 \cdot 10^{-4}$ sec.

The assumption that $\mathrm{RTT}_0 = 0$ is questionable. This off-set value of the round trip time is largely determined by the so-called packetizing delay, and can be considered fixed in the back-to-back modem pair set-up of this paper.

As an abstraction, it might be desirable to view the ADSL connection as a whole as a byte stream channel. This channel will have a byte error rate associated to it, which is exactly q as calculated. Note however, that byte errors on this channel will definitely not be uncorrelated, errors will appear in groups corresponding to data words.

	$R=0$	2	4	6	8	10	12	14	16
$S=1$	*	*	*	0.856	0.846	0.815	0.785	0.754	0.723
$S=2$	*	*	*	0.264	0.891	0.892	0.877	0.862	0.846
$S=4$	*	*	*	*	*	0.888	0.922	0.915	0.908
$S=8$	*	*	*	*	*	*	0.620	0.921	0.937
$S=16$	*	*	*	*	*	*	*	*	0.169

TABLE 3. η_{TCP} for $p = 0.001$, $\mu = 262144$ bytes/s, $D = 64$.

A. List of symbols

- μ Bandwidth in bytes/s: number of bytes per second that are transmitted over the physical link.
- N Number of bytes in an ADSL frame.
- n Number of bytes in a code word.
- K Number of data bytes in an ADSL frame.
- k Number of data bytes in a code word.
- R Number of redundancy bytes added to a code word for error correction. Admissible values for R are $(0, 2, 4, 6, 8, 10, 12, 14, 16)$.
- D Interleave depth. Admissible values for D are $(1, 2, 4, 8, 16, 32, 64)$.
- S Number of Mux frames to be encoded in one code word. Admissible values for S are $(1, 2, 4, 8, 16)$.
- e Number of errors that can be corrected in a code word
- L Length of a burst of errors in bytes.
- g Number of bytes in a TCP packet.
- η_{ADSL} Number of data bytes divided by the number of transmitted bytes through the ADSL modem.
- η_{TCP} Long time average fraction of data byte rate and the maximum byte rate (using TCP and an ADSL modem).

REFERENCES

1. *Asymmetric Digital Subscriber Line (ADSL) Metallic Interface*, T1E1.4/97-007R6, ANSI, 26 september, 1997
2. Performance Analysis of Window-based Flow Control using TCP/IP, T.V. LAKSHMAN and U. MADHOW, *High Performance networking V*, Vol. C-26, 135–149, 1994.
3. Modelling TCP Throughput: a Simple Model and its Empirical Validation, J. PADHYE, V. FIROIO, D. TOWSLEY, J. KUROSE, *Proceedings of SIGCOMM 98.*
4. The Macroscopic behavior of the TCP Congestion Avoidance algorithm, M. MATHIS, J. SEMKE, J. MAHDAVI, and T. OTT, *Computer Communications Review*, 27(3), 1997.
5. The Effect of Asymmetry on TCP Performance, H. BALAKRISHAN, V. PADMANABHAN, and R. KATZ, *Proc. 3rd ACM/IEEE Mobicom*, september 1997.

33rd European Study Group with Industry
14 – 18 September 1998

pp. 27 – 35

Laser Drilling

F. van Beckum, J.B. van den Berg, S.J. Chapman,
P. Hemker, J. Jansen, R. Mattheij, T. Myers,
M. Peletier, F. Quirós, K. Verhoeven

Report prepared by S.J. Chapman and K. Verhoeven

1. Introduction

Since the first demonstrations of the ruby laser in 1960, the laser quickly took an important place in various domains of industry. This is mainly because of its concentrated and contactless energy supply. This has led to many applications in the domain of laser materials processing. The most important applications in this domain are cutting, welding and marking. Laser drilling, the topic of this article, is a niche application.

Laser percussion drilling (drilling by multiple shots) is for instance used in the process of gas turbine manufacturing, because of the fact that the components to be drilled are made of superalloys which are very hard to machine by conventional techniques. To fix ideas, the typical hole diameter, hole depth and pulse length are $0.5 \div 1.0$ mm, $3 \div 10$ mm and 1.0 ms, respectively. Laser percussion drilling is favoured over alternative drilling processes like spark erosion drilling and laser trepanning drilling because it is by far the fastest process. However, it suffers of problems with the quality of the hole. The main quality aspects are:

- Tapering (Decrease of hole diameter with depth)
- Recast layer (Re-solidified material at wall of hole)
- Bellow shape (Local increase of hole diameter)

The laser drilling process depends on the material properties and on the laser beam characteristics: wavelength and intensity as a function of space and time.

The main goal of the research being started at the study group is to come up with a simulation model based on a mathematical model which includes all relevant physical features. This model is needed to get a better understanding of the process and to be able to select proper settings of the process parameters. Once well validated, this model will be used to define the specification of the ideal laser used for drilling. The major problem will be to handle the different phases and in particular the modelling of the interaction of the beam with the vapour phase.

The setup of this article is as follows. Sections 2 to 4 are concerned with the phase transformations of the material irradiated. In Section 5 the fact that drilling velocities are found to be much higher than can be accounted for by vaporization only is explained by the so called piston mechanism. Then,

I	$15 \cdot 10^9$	W m^{-2}
ρ	$2.70 \cdot 10^3$	kg m^{-3}
L_v	$11723.040 \cdot 10^3$	J kg^{-1}
L_f	$355.878 \cdot 10^3$	J kg^{-1}
k	229.111	W m^{-1} K^{-1}
c	896	J kg^{-1} K^{-1}
T_m	931.15	K
T_v	2543.15	K
μ	$2.66 \cdot 10^{-3}$	Pa s

TABLE 1. Physical data for drilling Aluminium. (These data were taken from [4])

Section 6 gives a few ideas on how to model the interactions of the incoming laser beam with the vapour phase in front of the target. Finally, Section 7 gives some conclusions and recommendations.

2. Evaporation-controlled limit

The simplest case to consider is the situation in which all the energy supplied to the surface goes into vaporizing the material, as in [1]. This evaporation-controlled limit may arise either when the energy is applied to the surface too rapidly for the heat to be conducted into the material, or when the beam power density is constant and the temperature ahead of the evaporating boundary approaches a steady state. By equating the rate of input of energy to the rate of absorption of latent heat of vaporization, we find

$$I = v\rho L_v. \tag{1}$$

This gives the velocity of the vaporization boundary as

$$v = \frac{I}{\rho L_v}. \tag{2}$$

Table 1 lists the physical constants relevant to the problem for aluminium (a material for which they were readily available). Using these we find $v \approx 0.5$ ms^{-1}.

Drilling by pure evaporation is observed in sublimating materials or in metals at low irradiance. In experiments drilling velocities of more than 1 ms^{-1} are found. Thus, at higher irradiances, drilling velocities are found to be much higher (perhaps by factors of $2 \div 5$) than can be accounted for by evaporation alone. It is clear that some of the material must be ejected from the drilled hole in the liquid state, probably via the splashing mechanism that relies on the evaporation pressure (or recoil pressure), described by Von Allmen [2, 3]. Therefore, we now address the question of the size of the melt pool which forms during the pre-vaporization "warm up" phase.

3. The melting model

The temperatures in both the liquid and the solid region are governed by the heat equation. We concentrate on diffusion of heat in the direction of drilling,

neglecting radial diffusion. For typical drilling parameters, this is shown in [1] to be a reasonable approximation.

Thus we have the following one-dimensional model

$$k_i \frac{\partial^2 T_i}{\partial x^2} = \rho c_i \frac{\partial T_i}{\partial t} \quad \text{in } \Omega_i \qquad \text{for } i = s, l, \tag{3}$$

where k, ρ and c are the thermal conductivity, density and specific heat capacity respectively, and the subscripts s and l denote the solid and the liquid. Furthermore, Ω_l denotes the liquid region $0 \leq x < x_0(t)$ and Ω_s the solid region $x_0(t) < x < \infty$ where $x_0(t)$ is the position of the solid-liquid interface defined by $T(x_0(t), t) = T_m$. At the the boundary $x = 0$ the energy is supplied,

$$k_l \frac{\partial T_l}{\partial x} = -I \qquad \text{at } x = 0. \tag{4}$$

At the solid-liquid interface the so called Stefan condition and continuity of temperature hold, yielding

$$k_l \frac{\partial T_l}{\partial x} - k_s \frac{\partial T_s}{\partial x} = -v_n L_f \rho \qquad \text{at } x = x_0(t), \tag{5}$$

$$T = T_m. \tag{6}$$

Here, v_n is the velocity of the interface in normal direction, where the normal $\mathbf{n}$ is the normal pointing into the solid and furthermore, L_f is the latent heat of fusion. At infinity, the boundary condition

$$T_s \to T_0 \qquad \text{as } x \to \infty \tag{7}$$

holds, where T_0 is the ambient temperature of the material. We nondimensionalize this by introducing the dimensionless variables $\overline{x}$, $\overline{t}$ and $\overline{T}$, defined by

$$x = x^* \overline{x} \;=\; \frac{k(T_v - T_m)}{I} \overline{x}, \tag{8}$$

$$t = t^* \overline{t} \;=\; \frac{\rho c k (T_v - T_m)^2}{I^2} \overline{t}, \tag{9}$$

$$T \;=\; T_m + (T_v - T_m)\overline{T}, \tag{10}$$

where we have assumed that k and c take the same values in the solid and liquid phases. Using the material data for aluminium gives the length and time scales $x^* \approx 2.5 \cdot 10^{-5}$m and $t^* \approx 6.4 \cdot 10^{-6}$s. Writing the equations together with the boundary conditions in dimensionless form we obtain the Stefan problem

$$\begin{cases} \dfrac{\partial^2 \overline{T}}{\partial \overline{x}^2} = \dfrac{\partial \overline{T}}{\partial \overline{t}} & \text{in } \Omega_i \quad i = s, l, \\ \dfrac{\partial \overline{T}}{\partial \overline{x}} = -1 & \text{at } \overline{x} = 0, \\ \overline{T} = 0; \;\; \left[\dfrac{\partial \overline{T}}{\partial \overline{x}}\right] = -\overline{L}_f v_n & \text{at } \overline{x} = \overline{x}_0(t), \\ \overline{T} \to \overline{T}_0 & \text{as } \overline{x} \to \infty, \end{cases} \tag{11}$$

where $\overline{L}_f = \frac{L_f}{c(T_v - T_m)}$ is the dimensionless latent heat of fusion, $\overline{T}_0 = \frac{T_0 - T_m}{T_v - T_m}$, and $\overline{x}_0(t)$ is the dimensionless position of the solid/liquid interface. With the material properties of aluminium we find $\overline{L}_f \approx 0.25$ (in fact $\overline{L}_f$ is small in almost all metals). In this case as a first approximation we can neglect the discontinuity in the temperature gradient due to the solid-liquid phase transition. This leads to the following problem

$$\begin{cases} \dfrac{\partial^2 \overline{T}}{\partial \overline{x}^2} = \dfrac{\partial \overline{T}}{\partial \overline{t}} & \text{in } \overline{x} > 0, \\ \dfrac{\partial \overline{T}}{\partial \overline{x}} = -1 & \text{at } \overline{x} = 0, \\ \overline{T} \to \overline{T}_0 & \text{as } \overline{x} \to \infty. \end{cases} \tag{12}$$

with solution [1]

$$\overline{T}(\overline{x}, \overline{t}) = 2\left(\frac{\overline{t}}{\pi}\right)^{\frac{1}{2}} \exp\left(-\frac{\overline{x}^2}{4\overline{t}}\right) - \overline{x}\ \operatorname{erfc}\left(\frac{\overline{x}}{2\overline{t}^{\frac{1}{2}}}\right) + \overline{T}_0. \tag{13}$$

To determine the time at which the surface starts to vaporize, we note that

$$\overline{T}(0, \overline{t}) = 2\left(\frac{\overline{t}}{\pi}\right)^{\frac{1}{2}} + \overline{T}_0, \tag{14}$$

and that vaporization begins when $\overline{T}(0, \overline{t}) = 1$, i.e. $\overline{t} = (1 - \overline{T}_0)\pi/4$. The dimensionless melt pool depth is given by $\overline{x}_0(t)$, defined by $\overline{T}(\overline{x}_0(t), \overline{t}) = 0$, giving

$$2\left(\frac{\overline{t}}{\pi}\right)^{\frac{1}{2}} \exp\left(-\frac{\overline{x}_0^2}{4\overline{t}}\right) - \overline{x}_0\ \operatorname{erfc}\left(\frac{\overline{x}_0}{2\overline{t}^{\frac{1}{2}}}\right) = -\overline{T}_0. \tag{15}$$

However, from the small length and time scales it follows that vaporization takes place very quickly and the melt pool is very small as vaporization starts. Hence if the melt pool splashes out as soon as vaporization begins it must do so many times per laser pulse, with a tiny amount of melt ejected each time.

Let us now consider the contrasting situation in which there is no immediate splash, to determine the maximum possible size of the melt pool ahead of the evaporating boundary.

4. Evaporation and melting

Once the material starts to vaporize the (dimensionless) Stefan problem (11) needs to be modified to include a Stefan condition and temperature condition at the vaporizing boundary. In dimensionless form these are given by

$$\frac{\partial \overline{T}}{\partial \overline{x}} = -1 + \frac{v_v}{\varepsilon}; \quad \overline{T} = 1. \tag{16}$$

where, $\varepsilon = \frac{c(T_v - T_m)}{L_v}$ measures the ratio of the thermal energy required to heat the material from its melting point to its vaporization point to the latent heat of vaporization. In the case of aluminium we have $\varepsilon \approx 0.12$, and ε is small for most metals. Hence it is sensible to consider the limit of small ε. However, a rescaling is necessary, since the boundary condition implies that the vaporizing boundary is stationary on the present length-scales and time-scales. Thus we introduce $\tilde{x}$ and $\tilde{t}$ by defining

$$\overline{x} = \frac{\tilde{x}}{\varepsilon}, \qquad \overline{t} = \frac{\tilde{t}}{\varepsilon^2}. \tag{17}$$

The new length and time scales are then $x^*/\varepsilon \approx 10^{-4}$m and $t^*/\varepsilon^2 \approx 1.5 \cdot 10^{-4}$s. We now have

$$\begin{cases} \dfrac{\partial^2 \overline{T}}{\partial \tilde{x}^2} = \dfrac{\partial \overline{T}}{\partial \tilde{t}}, & \text{in } \Omega_i, \quad i = s, l, \\ \overline{T} = 1; \quad \varepsilon \dfrac{\partial \overline{T}}{\partial \tilde{x}} = -1 + v_v, & \text{at } x = \tilde{x}_1(t), \\ \overline{T} = 0; \quad \dfrac{\partial \overline{T}}{\partial \tilde{x}} = -\overline{L}_f v_l, & \text{at } x = \tilde{x}_0(t), \\ \overline{T} \to \overline{T}_0 & \text{as } \tilde{x} \to \infty, \end{cases} \tag{18}$$

where $\tilde{x}_1(t)$ is the dimensionless position of the vaporizing boundary. The previous (pre-vaporization) problem corresponds to the small time behaviour of this problem. As $\overline{L}_f \to 0$, $\varepsilon \to 0$ the leading order problem is given by

$$\begin{cases} \dfrac{\partial^2 \overline{T}}{\partial \tilde{x}} = \dfrac{\partial \overline{T}}{\partial \tilde{t}} & \text{in material,} \\ \overline{T} = 1; \quad 0 = -1 + v_v & \text{at the vaporizing boundary.} \end{cases} \tag{19}$$

Hence $v_v = 1$ to leading order. This is exactly the evaporation limited solution that we found previously, and gives the dimensional speed of the vaporization boundary as $v_v \approx 0.7$ ms^{-1}. The solution for $\overline{T}$ is [1]

$$\overline{T}(\tilde{x}, \tilde{t}) = \left(\frac{1}{2} e^{-(\tilde{x} - \tilde{t})} \operatorname{erfc} \left(\frac{\left(\frac{1}{2}\tilde{x} - \tilde{t}\right)}{\tilde{t}^{\frac{1}{2}}} \right) + \frac{1}{2} \operatorname{erfc} \left(\frac{\tilde{x}}{2\tilde{t}^{\frac{1}{2}}} \right) \right) (1 - \overline{T}_0) + \overline{T}_0. \tag{20}$$

The position of the melt pool boundary $\tilde{x}_0(\tilde{t})$ is again given by $\overline{T}(\tilde{x}_0(\tilde{t}), \tilde{t}) = 0$, giving

$$\frac{1}{2} e^{-(\tilde{x}_0 - \tilde{t})} \operatorname{erfc} \left(\frac{\left(\frac{\tilde{x}_0}{2} - \tilde{t}\right)}{\tilde{t}^{\frac{1}{2}}} \right) + \frac{1}{2} \operatorname{erfc} \left(\frac{\tilde{x}_0}{2\tilde{t}^{\frac{1}{2}}} \right) = -\frac{\overline{T}_0}{1 - \overline{T}_0}. \tag{21}$$

For large times we find

$$\tilde{x}_0(\tilde{t}) \sim \tilde{t} + \log \left(\frac{1 - \overline{T}_0}{\overline{T}_0} \right). \tag{22}$$

Since $\tilde{x}_1 = \tilde{t}$, it follows that the size of the melt pool $\tilde{x}_0 - \tilde{x}_1$ approaches (from below) the constant value

$$\log\left(\frac{1-\overline{T}_0}{\overline{T}_0}\right)$$

as the vapourization proceeds. This gives the maximum size of the melt pool available for ejection through splashing.

5. The piston mechanism

As we have already noted, at high irradiances drilling velocities in metals are often found to be much higher than can be accounted for by evaporation only. The reason is that much of the metal extracted leaves the hole as melt rather than as vapour. One mode of melt ejection is the piston mechanism as illustrated in Figure 1, in which the melt is squirted out of the hole by the recoil pressure at the evaporating boundary. We could now ask ourselves the question

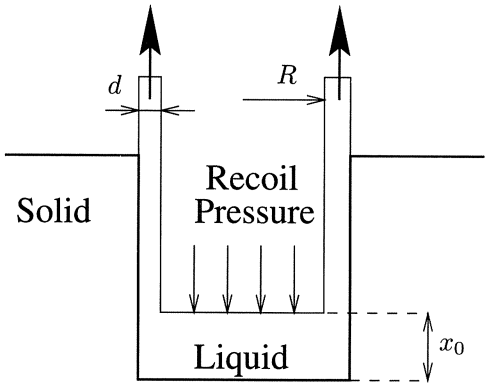

FIGURE 1. The piston mechanism.

as to how quickly does the fluid get expelled by the recoil pressure.

We obtain this velocity by balancing the forces. The work done by the recoil pressure, assuming that the total amount of liquid drawn in Figure 1 is squirted out, is

$$p\pi R^2 x_0. \tag{23}$$

If the fluid is expelled quickly (which can be verified a posteriori) the flow will be high Reynolds number, and we can neglect viscous dissipation. Then this energy will all be converted to kinetic energy, i.e.

$$\left(\frac{1}{2}\rho u^2\right) \times \pi R^2 x_0. \tag{24}$$

This gives the velocity,

$$u = \left(\frac{2p}{\rho}\right)^{\frac{1}{2}}. \tag{25}$$

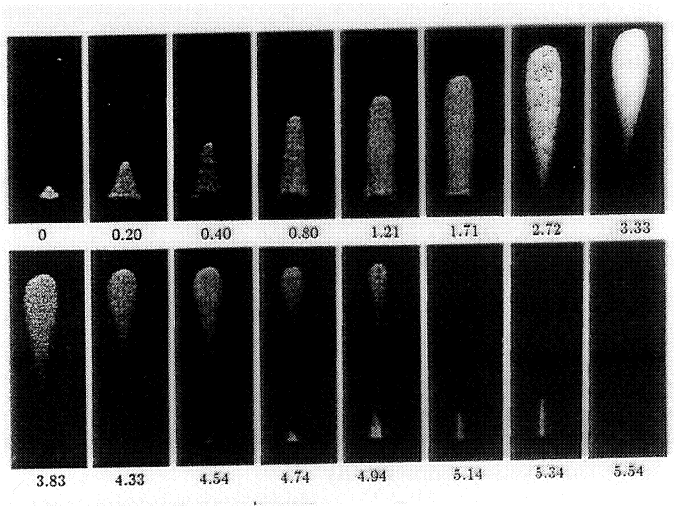

FIGURE 2. High-speed camera frames of a vapour cloud from an aluminium alloy irradiated by 5 ms, 1.5MW/cm^2 CO_2-laser pulses (incident from above). Blocking of the incoming radiation by the plume can be seen. Numbers below the frames give the time in ms.

VON ALLMEN [3] gives an example in which a speed up to 50 ms^{-1} is reached. Assuming this speed in the case of aluminium would give a Reynolds number of

$$\mathrm{Re} = \frac{\rho u L}{\mu} \approx 5 \cdot 10^4, \tag{26}$$

where L is the characteristic length (1 mm). This supports the assumption of neglecting viscous dissipation.

6. THE VAPOUR MODEL

In the previous sections one of the assumptions used to derive the models was the transparency of the vapour. In many cases, especially considering irradiations in the intensity regime used to drill, this assumption is not valid, as can be seen in Figure 2. In this figure it is easy to see that the vapour plume absorbs the incoming radiation by noting that this plume shields the target completely (frames 8 to 10). Therefore a model has to be made that also takes into account the absorption of incoming energy by the vapour plume in front of the target. Possible first steps towards such a model are presented in this section. Section 6.1 takes this step by using conservation of both mass and momentum, whereas section 6.2 uses the so called Rankine-Hugoniot approach, that is, one models the vapour as a shock wave.

6.1. Balance Equations

First we try to model the vapour in one dimension where we define $x = 0$ to be the top of the hole and $x = h$ to be the depth of the hole. Conservation of mass and of momentum give us

$$\frac{\partial \rho}{\partial t} + \frac{\partial}{\partial x}(\rho u) = 0, \tag{27}$$

$$\frac{\partial}{\partial t}(\rho u) + \frac{\partial}{\partial x}(\rho u^2) + \frac{\partial p}{\partial x} = 0, \tag{28}$$

respectively. Here, u is the speed of the vapour ρ is its density and p is the pressure. Furthermore we assume the mass-flux ρu to be given at $x = h$, and the density ρ and the pressure p to be the ambient density ρ_0 and ambient pressure p_0 at $x = 0$, respectively.

If we assume the vapour to be an ideal gass, a rather crude assumption, we are able to solve this system numerically.

This model has to be extended by including an equation that models the absorption of radiation by the vapour and by an equation that models the temperature rise of the vapour as a function of the absorbed intensity. With this model we can compute the amount of energy that reaches the bottom of the hole, and therefore can be used to determine the time at which the target is shielded by the vapour.

6.2. The Rankine-Hugoniot Approach

Another approach to model the vapour makes use of the idea that the front of the vapour plume can be modelled as a density shock wave. Denote the conditions in front of the shock wave by the subscript $-$ and the conditions after the shock wave by the subscript $+$. Using the assumption that the vapour can be modelled as an ideal gass, the so-called Rankine-Hugoniot relations are given by

$$[\rho]\dot{s} + [\rho u] = 0, \tag{29}$$

$$[\rho u]\dot{s} + [\rho u^2 + RT\rho] = 0. \tag{30}$$

Here, $x = s(t)$ denotes the position of the shock, and $[\,\cdot\,]$ denotes the jump across the shock. This leads to

$$\frac{[\rho u]}{[\rho]} = \frac{[\rho u^2 + RT\rho]}{[\rho u]}. \tag{31}$$

Assuming $u_- = 0$ leads to

$$\rho_+(\rho_+ - \rho_-)^2 = \frac{\rho_-(\rho_+ u_+)^2}{RT}. \tag{32}$$

Knowing the mass flux $\rho_+ u_+$ and ρ_- this equation fixes ρ_+ and thereby u_+. Now we can compute the speed of the shock wave by

$$\dot{s} = -\frac{[\rho u]}{[\rho]}. \tag{33}$$

7. Conclusions and Remarks

We have examined various aspects of the laser drilling process. We first examined the simplest case of the evaporating-controlled limit, in which all the energy supplied by the laser is used in vaporizing the material. This predicts drilling velocities lower than those observed in experiments, which leads to the conclusion that some of the material removed from the hole must be ejected in a liquid state rather than in a vapour state.

We therefore turned our attention to the size of the melt pool which is formed during the drilling process. We found that in the "warm up" stage before vaporization begins the melt pool formed is very small, so that if it is splashed out immediately the surface starts to vaporize there must be a high frequency of very small splashes.

We then considered the case in which the melt is not splashed out immediately, but remains for a while as vaporization is taking place. We found that the melt pool increases in size considerably up to a maximum value which is easily calculated. However, during this vaporization phase most of the energy supplied to the surface of the irradiated material goes into vaporization, with only a small amount being used to create the melt pool.

Since it is more efficient to splash out melt than to vaporize it, improved control of the melt pool may lead to more efficient drilling. One possibility is to try to generate a large melt pool with a minimum of evaporation by applying a relative low intensity pulse, followed by a high intensity pulse to generate high evaporation producing the recoil pressure to splash out this melt pool. This may also help to minimize the recast layer formed by the collapse of the final splash when the hole breaks through the material, since the melted region will break through before the final splash and the final melt will be ejected through the hole rather than back.

Although the studygroup came to some results for the process of absorption of energy in the vapour plume in front of the target, and the two different approaches to tackle the absorption presented in this article are promising, this topic needs further research and a more sophisticated modelling. Furthermore, experimental results have to be obtained to validate the vaporization models.

References

1. J.G. Andrews & D.R. Atthey, *On the motion of an intensely heated evaporating boundary.* J. Inst. Maths. Applics. **15**, 59–72 (1975).
2. M. von Allmen, *Laser drilling velocity in metals*, Journal of Applied Physics, **47**, no. 12, pp. 5460–5463 (1976).
3. M. von Allmen & A. Blatter, *Laser-beam interactions with materials*, Springer-Verlag, Berlin, (1995).
4. K. Ražnjević, *Handbook of thermodynamic tables and charts*, McGraw-Hill, New York, (1976).

33rd European Study Group with Industry
14 – 18 September 1998
pp. 37 – 53

Thermally Pressing Corner Profiles

Tim Myers
Sjoerd W. Rienstra
TU Eindhoven
Department of Mathematics
P.O. Box 513 5600 MB Eindhoven, The Netherlands

with contributions from:

Jon Chapman, Warrick Cooke, Christian van Enckevort,
Michael Lee, Chris Stolk, Fons van de Ven.

1. Introduction

Trespa International B.V. (Weert, The Netherlands) is a manufacturer of high quality panel material for exterior and interior uses, made of polymerized resin, reinforced with wood fibres or sulphate paper. Typical applications are office desk tops and facade cladding.

The production process starts with impregnating large sheets of paper with resin. Then a pile of sheets of 8–13 mm is pressed together under high pressure (90 bar) in a mould until all of the air is squeezed out. In simplistic terms, the pressing of a plate occurs in two distinct stages; compression followed by heating. This is depicted in Figure 1, where the curves show the product

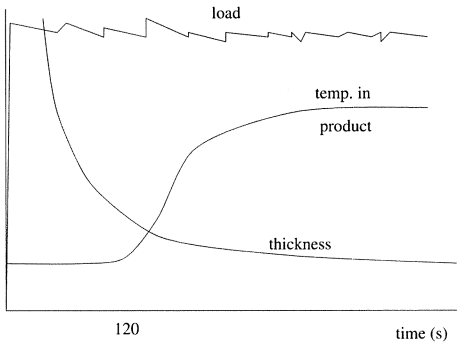

Figure 1. Typical thickness, temperature and loading curves.

thickness, temperature and applied load over time. During the first stage of the process, which last approximately two minutes, the components are compressed to within 10% of the final thickness. During this stage very little heat has reached the components. During the second stage the temperature reaches a critical value and the resin starts to polymerize, eventually resulting in the

solidification of the melt. During polymerization water is formed, which is partly dissolved in the polymer and fibers, partly squeezed out sideways, and partly evaporated through the upper and lower surfaces.

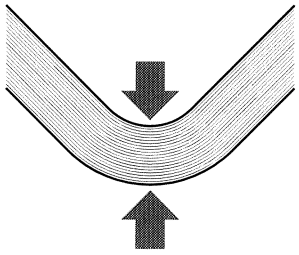

FIGURE 2. The corner profile

The majority of the production involves the manufacture of large rectangular flat plates. Here, the process is well controlled, with little failure losses. A minority of the production consists of, so-called, corner profiles, where a two-dimensional corner (legs of 30 cm, a lateral extension of 4 m) is made by heat-pressing a pile of sheets, folded into a corner shaped mould (figure 2). The upper and lower surfaces of the legs are not exactly parallel. The angle between the legs of the inner mould is 90°, and of the outer mould 91.5°, which is a small but critical amount more. In this way the mould slightly diverges, such that it closes first in the corner, while the contact area between the sheets moves from the corner into the legs. The legs are connected by circular arcs of 10 mm (inner) and 20 mm (outer) radius. This shape may be modified if necessary.

The process of pressing a corner profile is less stable than the regular flat panel process. Density variations and surface blisters have been observed that are supposedly due to captured air and water.

The question is to explain or clarify, by suitable mathematical modelling, the physical processes leading to this adverse behaviour, and to suggest (ways to obtain) more favourable mould shapes.

2. MODELS

We will adopt the hypothesis here that the reduced structural quality is primarily caused by captured air bubbles and not, for example, by chemical changes of material. Therefore, the models used will be centered around the mechanical side of the processes, where bubbles might play a rôle. They are described by the fluid mechanical (resin) and elasto-mechanical behaviour (polymer) of the material.

It is believed that the bubbles are trapped mainly because, when compressed, the material closes in such a way that the induced pressure is not conducive to expelling the trapped air. A description of the actual trapping of bubbles is evidently very difficult, as it requires a kinematical or even dynamical model of a non-continuous material. A better approach, feasible but

requiring a more in-depth research, would be a mixture model [7]. For the moment, however, we will remain, for simplicity, with single component models, probably valid when the trapped air bubbles are small. Therefore, we will evaluate below the following two models: one describing the viscous flow part, and one describing the elastic solid part. At this moment it is not clear yet which description will be most relevant to the original questions. On the one hand, the flow of the heated resin and the trapping of bubbles is a process for which nothing but a viscous model appears to be appropriate. On the other hand, the resin polymerizes, and during the pressing process mainly air (and very little resin) is driven out of the (open!) sides, which suggests that a solid (elastic) model might be in order.

3. Viscous considerations

3.1. Introduction

As previously mentioned, the pressing occurs in two distinct stages, compression followed by curing. The following section is concerned only with the first part of the production process, the compressing stage. In particular the viscous flow of the resin is investigated. The first model described deals with the shearing effect caused by the relative motion of the paper sheets, to determine whether this can tear the paper and lead to cracks appearing. The second model deals with the viscous squeeze flow. The reason for studying this is that it is assumed a considerable part of the densification is due to air bubbles being forced out of the resin. This is backed up by experimental observations of vapor being ejected, although little resin is seen to be ejected. However, it is quite likely that the viscous resin is pushed into the paper and trapped (or at least considerably slowed down). Air bubbles may not take the same path, either because their surface tension makes it more difficult to push air through the narrow paper pores or that air may simply move more rapidly between the paper layers and so be more easily ejected before becoming trapped.

To remove trapped air bubbles the pressure gradient must be reasonably large and acting to push the fluid outwards, to force the bubbles through the viscous resin to the edge of the plates. For this reason the pressure profile in the resin layer is sought. The complication of the resin being forced into the paper is not investigated here, however, an analysis of this situation may be found in [1].

3.2. Cracking due to shear?

During compression of a corner piece there must be some relative motion of the paper layers as the composite adjusts from a flat shape to a curved one. The only significant force opposing this motion is the viscous resistance of the resin. In this section an order of magnitude study is carried out to determine whether this shear force is sufficient to tear the paper and so produce cracks in the finished product.

Geometrical considerations indicate that the relative distance, L, moved by

two adjacent sheets of paper bending to a right angle is

$$L \sim \tfrac{1}{4}\pi(r_2 - r_1), \tag{1}$$

where r_1 and r_2 are the radii of curvature of the paper sheets. In the current

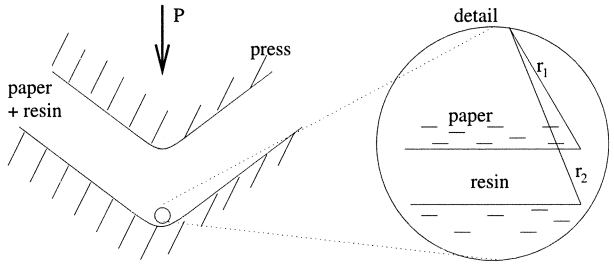

FIGURE 3. Geometry for pressing a corner piece.

problem the radius of curvature of the corner is typically 10 mm, the thickness of the resin layer is 10 μm. Hence locally the problem can be considered as one of Couette flow, see Figure 3. In which case standard viscous flow theory indicates that the shear stress in the fluid is constant and given by

$$\tau = \frac{\eta U}{H}, \tag{2}$$

where η is the viscosity and H is the distance between the two surfaces, $H \sim r_2 - r_1$. The velocity U is given by the length-scale L divided by the time-scale for the flow, which is here taken as 10 s. This leads to

$$\tau = \frac{\eta}{H}\frac{\pi \cdot H}{4 \cdot 10} = \frac{\pi\eta}{40}, \tag{3}$$

so the shear stress is independent of the layer thickness. A typical value for the resin viscosity is 2000 cP or 2 Pa s, so the shear stress is of the order 0.16 N/m. Trespa quote the breaking stress of the paper used in the pressing process as 20×10^6 N/m^2, a sheet of thickness 100 μm therefore requires 2×10^3 N/m to tear it. The analysis therefore shows that the stress caused by the shearing of the resin is considerably smaller than that required to tear the paper and it is highly unlikely cracks will appear due to this mechanism.

3.3. Viscous squeezing problem

As the plates compress the resin/paper composite a viscous squeeze film will occur between each pair of paper sheets and the resin will be forced either into the sheets or outwards. To understand the compression of the composite, it is first necessary to understand the basic component of the system, a fluid being squeezed by the normal motion of two solid surfaces. This is the focus of the present section. The main aim of the analysis is to determine the pressure gradient within a resin layer, since this will act to expel (or retain) air bubbles.

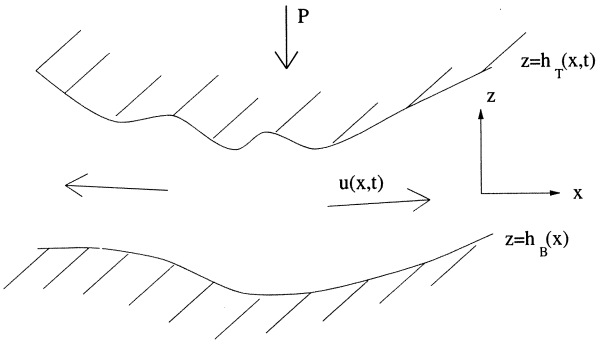

FIGURE 4. A viscous fluid squeezed between two plates located at $z = h_T(x,t)$, $z = h_B(x)$.

Consider the problem of a viscous fluid being squeezed between two solid surfaces, as depicted in Figure 4. Without loss of generality the bottom surface can be assumed stationary, whilst the top one moves under a load P, which may vary with time.

In 2-D the standard lubrication approximation reduces the Navier-Stokes equations to

$$\frac{\partial p}{\partial x} = \eta \frac{\partial^2 u}{\partial z^2}, \tag{4}$$

$$\frac{\partial p}{\partial z} = 0. \tag{5}$$

The continuity equation remains unchanged under this approximation:

$$\frac{\partial \rho}{\partial t} + \frac{\partial (\rho u)}{\partial x} + \frac{\partial (\rho w)}{\partial z} = 0\,. \tag{6}$$

Appropriate boundary conditions for the velocities u and w are

$$u(h_T) = u(h_B) = 0, \tag{7}$$

$$w(h_B) = 0, \qquad w(h_T) = \frac{\partial h_T}{\partial t}\,, \tag{8}$$

where $h_T(x,t)$ and $h_B(x)$ are the positions of the top and bottom surfaces. Equations (7) and (8) specify no-slip on the solid surfaces. The pressure must be ambient at either end of the contact, *i.e.* $p(\pm L) = p_a$. In the following the ambient pressure will be set to zero. The total load P is the integral of the pressure over a surface $P = \int_{-L}^{L} p(x)\,\mathrm{d}x$. The density is assumed to depend only on pressure and so $\rho(\pm L) = \rho_a$.

Equation (5) indicates $p = p(x,t)$ and hence $\rho = \rho(p) = \rho(x,t)$. Equation (4) may be integrated immediately to give the velocity

$$u = \frac{1}{2\eta}\frac{\partial p}{\partial x}(z - h_B)(z - h_T). \tag{9}$$

Integrating the continuity equation between $z = h_T$ and h_B leads to

$$\frac{\partial \rho}{\partial t}(h_T - h_B) + \frac{\partial}{\partial x}\Big[\rho \int_{h_B}^{h_T} u \, \mathrm{d}z\Big] + \rho \frac{\partial h_T}{\partial t} = 0. \tag{10}$$

Substituting for the velocity and rearranging provides the governing equation for the squeeze flow of a compressible fluid:

$$\frac{\partial}{\partial t}\Big[\rho(h_T - h_B)\Big] = \frac{\partial}{\partial x}\Big[\frac{\rho}{12\eta}\frac{\partial p}{\partial x}(h_T - h_B)^3\Big]. \tag{11}$$

For all cases the dependence of the heights on x should be known (the shape of the press) and for simple configurations equation (11) may be solved analytically. Three such scenarios are worked through in the following sections. However, in general, equation (11) will require solving numerically, this is not carried out in the present work.

Incompressible flow between flat plates

To illustrate the method described above, the simplest configuration, that of an incompressible squeeze film between two flat plates, will be described in this section. In which case the position of the plates is described by

$$h_B = 0, \qquad h_T = h(t), \tag{12}$$

and equation (11) reduces to

$$\frac{\partial h}{\partial t} = \frac{\partial}{\partial x}\Big(\frac{h^3}{12\eta}\frac{\partial p}{\partial x}\Big). \tag{13}$$

Since $h = h(t)$ this may be integrated immediately. After applying the symmetry condition $\partial p/\partial x = 0$ at $x = 0$, this gives an expression for the pressure gradient:

$$\frac{\partial p}{\partial x} = \frac{12\eta f x}{h^3}\,, \tag{14}$$

where $f = \partial h/\partial t$. This shows that the pressure gradient increases linearly away from the centre, $p \propto x$. The consequence for bubble motion through the resin is that near the centre there will only be a small force to cause movement and this is where bubbles are most likely to be trapped. Away from the centre the force increases and so bubbles near the edge of a plate are likely to be removed relatively rapidly.

The pressure in the resin can be determined by integrating (14), subject to $p(\pm L) = 0$:

$$p(x,t) = \frac{6\eta f}{h^3}(x^2 - L^2). \tag{15}$$

This still involves the unknown function $f(t)$ which must be determined by the load condition

$$P = \int_{-L}^{L} p \, \mathrm{d}x = -\frac{8\eta f}{h^3}L^3. \tag{16}$$

So the pressure at any time t is given by

$$p(x,t) = \frac{3P}{4L^3}(L^2 - x^2). \tag{17}$$

Note that the load P applied to the top plate is a known quantity, which may vary with time. The film thickness at time t is determined by integrating f. For the case of constant load this leads to the classical expression for the height variation of an incompressible squeeze film

$$h(t) = \left(\frac{1}{h_0^2} + \frac{Pt}{4L^3\eta}\right)^{-1/2}, \tag{18}$$

see [2, 3] for example. With a time-dependent load, as is depicted on Figure 1, the film height equation requires solving numerically.

Another classic example of a squeeze film is the converging/diverging bearing. The diagrams of presses provided by Trespa indicate that this is also a relevant situation to study, however since the analysis is similar to that described above it is not worked through here. The main result of interest is that the pressure in a converging bearing is similar to that of equation (17) but flattened in the centre and steeper near the edges. Consequently, the central pressure gradient is less favourable to removing air bubbles than the flat plate. A diverging profile has the opposite effect.

Quadratic profile plates

As an approximation to the true shape of the plates when manufacturing a corner the relatively simple case of a quadratic profile will be considered in this section:

$$h_T = h(t) + bx^2 \tag{19}$$

$$h_B = ax^2 \ . \tag{20}$$

If the corner sections are thought of as approximately circular, as depicted in Figure 3, with radii r_1 and r_2 then $b \sim 1/2r_1$, $a \sim 1/2r_2$. The physical case of interest to the present study has $r_1 < r_2$, so $a < b$. Again the fluid will be assumed incompressible. To simplify the analysis the z co-ordinate will be shifted to $\zeta = z - bx^2$, so

$$h_T = h(t) \tag{21}$$

$$h_B = (a-b)x^2 = Bx^2 \ . \tag{22}$$

Equation (11) may be integrated, subject to a symmetry condition at $x = 0$, to give the following expression for the pressure gradient:

$$\frac{\partial p}{\partial x} = \frac{12\eta f x}{(h - Bx^2)^3} \ . \tag{23}$$

Due to the symmetrical nature of the problem, the pressure gradient must always be zero at the centre and bubbles are likely to be retained here. Away

from the centre equation (23) shows that when $B > 0$ the pressure gradient will decrease (since $f < 0$) monotonically away from the centre. The possible singularity, when $x = \sqrt{h/B}$, cannot occur since this implies the surfaces have come into contact, which is only possible in infinite time. When $B < 0$ the pressure gradient decreases away from the centre to a minimum at $x = \pm\sqrt{H/5|B|}$ after which it increases to an asymptote at $\partial p/\partial x = 0$. In this case the pressure gradient over most of the central region (except in the vicinity of $x = 0$) is large and should force air out rapidly. However, as the bubbles approach the edge of the contact region the pressure gradient becomes small and it is possible the bubbles may slow down sufficiently here and not be expelled.

Equation (23) can also be integrated analytically to provide an expression for the fluid pressure:

$$p(x,t) = -\frac{3\eta f}{B}\left[\frac{1}{(h-BL^2)^2} - \frac{1}{(h-Bx^2)^2}\right]. \tag{24}$$

As in the previous example this requires integrating to determine f in terms of the applied load P, which in this case is assumed constant. This leads to, for $B < 0$:

$$f = -\frac{P|B|}{3\eta}\frac{h\sqrt{h|B|}(BL^2+h)^2}{\arctan(L\sqrt{|B|/h})(BL^2+h)^2 - \sqrt{h|B|}L(-|B|L^2+h)}, \tag{25}$$

and for $B > 0$:

$$f = \frac{PB}{3\eta}\frac{h\sqrt{hB}(BL^2-h)^2}{\operatorname{arctanh}(BL/\sqrt{hB})(BL^2-h)^2 - \sqrt{hB}L(BL^2+h)}. \tag{26}$$

The position of the top plate is determined by numerical integration of $\partial h/\partial t = f$, with f given by either (25) or (26).

Quadratic/linear plates

As depicted in Figures 2 and 3, a corner profile is closely approximated by an approximately circular central region joined to an outer, straight section. This may be represented approximately by the form

$$\begin{aligned} h_T &= h(t) + bx^2 && |x| \le l \\ &= h(t) + 2al(|x|-l) + bl^2 && l \le |x| \le L \\ h_B &= ax^2 && |x| \le l \\ &= 2al(|x|-l) + al^2 && l \le |x| \le L\,. \end{aligned} \tag{27}$$

As in the previous section $b \sim 1/2r_1$, $a \sim 1/2r_2$ where r_1, r_2 are the inner and outer radii of curvature of the central region. Shifting the z-coordinate such that

$$\begin{aligned} \zeta &= z - bx^2 && |x| \le l \\ &= z - 2al(|x|-l) - bl^2 && l \le |x| \le L \end{aligned} \tag{28}$$

transforms the plate positions to

$$\begin{array}{lll} h_T = h(t) & & \forall x \\ h_B = (a-b)x^2 & & |x| \le l \\ \quad = (a-b)l^2 & l \le & |x| \le L\ . \end{array} \tag{29}$$

The problem is then reduced to a combination of those of the previous two sections.

Setting $B = a - b$ the pressure gradient in the two regions is determined as

$$\begin{aligned} \frac{\partial p}{\partial x} &= \frac{12\eta f x}{(h - Bx^2)^3} && |x| \le l \\ &= \frac{12\eta f x}{(h - Bl^2)^3} && l \le |x| \le L\ . \end{aligned} \tag{30}$$

Note, the discontinuity in the gradient of h_T and h_B at $x = l$ will be reflected in a discontinuity in the gradient of $\partial p/\partial x$. The corresponding pressure is

$$\begin{aligned} p &= -\frac{3\eta f}{B}\Big(\frac{1}{(h - Bl^2)^2} - \frac{1}{(h - Bx^2)^2}\Big) - \frac{6\eta f(L^2 - l^2)}{(h - Bl^2)^3} && |x| \le l \\ &= -\frac{6\eta f(L^2 - x^2)}{(h - Bl^2)^3} && l \le \quad |x| \le L. \end{aligned} \tag{31}$$

As $l \to 0$ equations (30, 31) reduce to the results for linear plates, as $l \to L$ the quadratic plate results are retrieved. The total load is, for $B < 0$,

$$\begin{aligned} P &= -\frac{3\eta f}{|B|}\frac{\arctan(|B|l/\sqrt{h|B|})(|B|l^2 + h)^2 - \sqrt{h|B|}l(-|B|l^2 + h)}{h\sqrt{h|B|}(|B|l^2 + h)^2} \\ &\quad -\frac{8\eta f(L^3 - l^3)}{(h + |B|l^2)^3}, \end{aligned} \tag{32}$$

for $B > 0$,

$$\begin{aligned} P &= \frac{3\eta f}{B}\frac{\operatorname{arctanh}(Bl/\sqrt{hB})(Bl^2 - h)^2 - \sqrt{hB}l(Bl^2 + h)}{h\sqrt{hB}(Bl^2 - h)^2} \\ &\quad -\frac{8\eta f(L^3 - l^3)}{(h - Bl^2)^3}. \end{aligned} \tag{33}$$

Since $f = \partial h/\partial t$ these provide the equation for the separation of the two plates $h(t)$, which must again be solved numerically.

3.4. Conclusion and results

In section §3.2 a simplified model for the shearing of a paper/resin system was analysed. Assuming Couette flow, an order of magnitude analysis indicates that cracking will not occur due to the shear of the very viscous resin. Since the induced stress is so much smaller than the required breaking stress it is clear that even if modifications are made to model the flow more accurately the changes will never result in a sufficiently large stress to tear the paper.

In §3.3 a squeeze film model is investigated in order to calculate the pressure within the resin. It is assumed that a sufficiently high pressure gradient will act to drive bubbles of trapped gas from the resin, leading to the appropriate densification. Three examples are worked through in §3.3-3.3. The first of these details the classical squeeze film between two flat plates. The problems described in the latter two sections cover quadratic profile plates and a combination of quadratic and linear ones. The analysis of the quadratic and

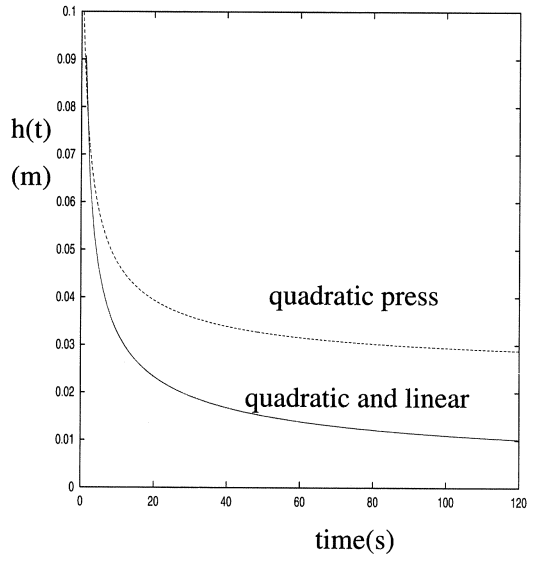

FIGURE 5. Variation of height $h(t)$ for first 120 s.

quadratic/linear profile problems led to an ordinary differential equation for the height $h(t)$, which required solving numerically. The pressure and pressure gradient may then be determined from equations (23, 24, 30, 31).

Figure 5 shows the variation of height $h(t)$ over time for a press with load $P = 100\,\mathrm{N}$, $L = 0.5\,\mathrm{m}$, $l = 0.25\,\mathrm{m}$ and $B = 0.1\,\mathrm{m}^{-1}$ for all three cases discussed earlier. As expected all the height curves decrease in a nonlinear fashion, with an initial rapid decrease followed by a long slow settling period. This is similar to the experimental height decrease displayed in Figure 1. Of the three curves the one corresponding to the linear plate settles most slowly, the quadratic plate settles most rapidly.

The pressure profiles are shown in Figure 6 at time $t = 120\,\mathrm{s}$. The problem of squeezing a fluid between two flat plates leads to a parabolic pressure profile, with a maximum at $x = 0$ of approximately $150\,\mathrm{Pa}$. The quadratic plates, in this example, give a very high pressure near the centre which decreases rapidly to an almost negligible value after $x = 0.35\,\mathrm{m}$. Decreasing the magnitude of B reduces the height of the central peak and increases the value at larger x, until, as $B \to 0$ the linear profile is retrieved. The combination of quadratic and linear plates leads to higher pressures than the purely linear case near the

centre and lower values further out.

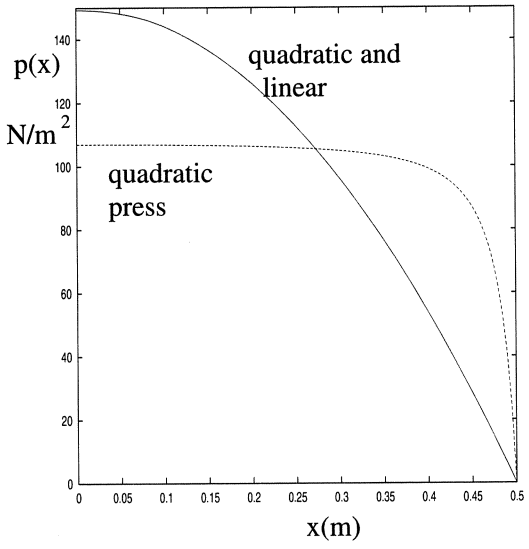

FIGURE 6. Pressure profiles during later stages of pressing process.

The quantity of greatest interest to the present study is the pressure gradient, this is depicted for the three cases in Figure 7. The flat plates show a linearly decreasing pressure gradient which will act to expel air more rapidly the further away it is from the centre. The quadratic plates give a very high pressure gradient over the central region (except in the close vicinity of $x = 0$), which will act to expel air very rapidly from this region. However, further out the pressure gradient becomes very small indicating the possibility of bubbles becoming trapped. Decreasing B will help alleviate this effect. Finally, the linear and quadratic combination incorporates the desirable features of the two separate cases. The pressure gradient is high near the centre. Following the trend of the quadratic plate profile, after reaching a minimum the magnitude decreases until the least effective point for removing air is reached where the linear profile is adopted. After this point the magnitude of the pressure gradient once again increases. With this form of plates there are therefore two likely places for bubble entrapment to occur. The first is at the centre where $\partial p/\partial x = 0$, the second is where the different profiles join and the magnitude of $\partial p/\partial x$ reaches a local minimum value. Adjusting the shape of the curve defined by B and the join position l this minimum value can be altered and so help prevent entrapment in this region. Preliminary calculations indicate that decreasing B (*i.e* making the corner tighter) or increasing l increases the central pressure gradient but reduces the pressure after the join. Increasing B or decreasing l has the opposite effect. The optimal choice will be one which gives an initial rapid rise in the magnitude of the pressure gradient but does not allow the gradient to become too small near the join.

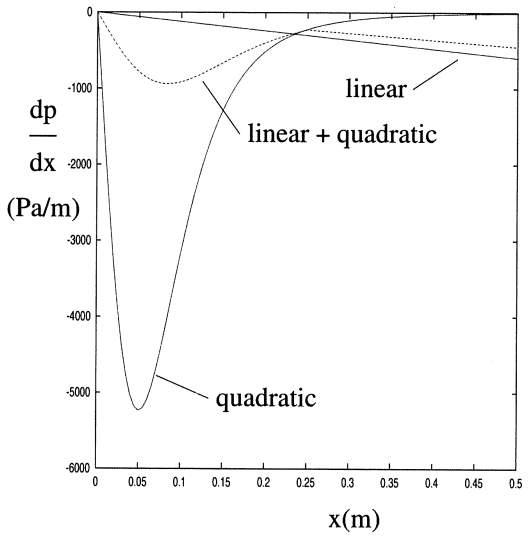

FIGURE 7. Pressure gradients during later stages of pressing process.

The consequences for a press with a converging or diverging form, have not been investigated, although the mathematical model has now been set up to permit this to be carried out relatively easily. However, work on purely converging systems indicates that a converging press will be more likely to entrap air. A diverging one will encourage air removal and this is the type used in practice by Trespa.

Equation (11) sets up the problem for a compressible fluid, however only incompressible examples have been used in the current study. There are two reasons for this, firstly the incompressible problem is considerably simpler, but the main reason is that to close the system a pressure density relation is required. At present there is no information on this. However, the incompressible flow model should indicate the correct trends for pressure and height variation. Further, it is not clear whether the actual fluid is compressed. The current study assumed that the compression effect was due to the removal of air from the resin, the resin will also permeate into the paper. A compressible model would just be imitating this behaviour.

The motion of the bubbles has also not been discussed, except in a very simple manner. Clearly an appropriate pressure gradient will act to move the bubbles, but a relation between the bubble velocity and pressure gradient is still required. To calculate this properly is beyond the scope of this work, however, it is likely that the bubble velocity will be of the same order as the resin velocity. The average resin velocity may be calculated from (9) as

$$\overline{u} = -\frac{\partial p}{\partial x}\frac{(h_T - h_B)^2}{12\eta}. \tag{34}$$

From this it may be estimated how long a bubble will take to travel from a

specified point to the plate edge.

4. Anisotropic elastic solid model

Since the compression or normal stress properties, affected by the captured air bubbles, are expected to be considerably different from the shear stress properties, affected by the layered structure of the paper sheets, the solid phase of the material will be modelled anisotropically, *i.e.* with different Young's moduli in crosswise and lateral directions.

Consider the following geometry (Figure 8). Because of symmetry we only have to consider one half of the profile. The planar part (the leg) occupies the region

$$0 \le x \le L, \quad 0 \le y \le a,$$

while the circular part (the corner area) is given by

$$\begin{aligned} x &= -r\sin(\theta+\theta_1), \quad y = -R + r\cos(\theta+\theta_1), \\ &-\theta_1 \le \theta \le 0, \quad R \le r \le R + a = R_a, \end{aligned}$$

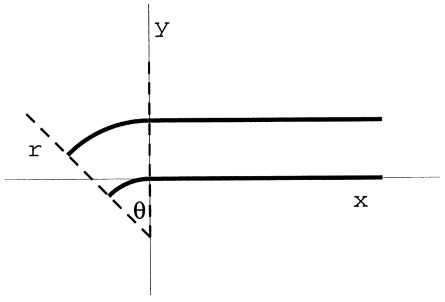

FIGURE 8. The geometry

where $\theta_1 = \frac{1}{4}\pi$, and R and a are typically 10 mm. The small variations on this geometry (leg angle, etc.), which are supposed to create favourable or unfavourable stress distributions, will for the moment be incorporated by appropriate boundary conditions.

We obtain for the stress tensor $\mathcal{T}$ (with elements t_{ij}) in the planar configuration the following constitutional stress-strain relations [8]

$$t_{xx} = E_L \frac{\partial \xi}{\partial x}, \quad t_{yy} = E_C \frac{\partial \eta}{\partial y}, \quad t_{xy} = G\Big(\frac{\partial \xi}{\partial y} + \frac{\partial \eta}{\partial x}\Big) \tag{35}$$

where $\xi \mathbf{e}_x + \eta \mathbf{e}_y$ is the displacement vector, and the Young's moduli in cross wise (E_C), lateral (E_L) and shear (G) direction are related by

$$2G < E_C \ll E_L.$$

t_{ij} is the stress applied at the side with normal $\mathbf{e}_i$ in direction $\mathbf{e}_j$. The Poisson contraction factor is assumed to be zero: $\nu = 0$. If the material were isotropic, we would have $2G = E_C = E_L$. Boundary conditions will be

$$\begin{array}{lllll} \text{at} & y & = & 0: & \xi = \eta = 0 \quad \text{(no slip)}, \\ \text{at} & y & = & a: & \xi = f(x), \quad \eta = -g(x), \\ \text{for} & x & \to & \infty: & \xi, \eta \to 0. \end{array}$$

A suitable first choice will be a simple displacement $f(x) = g(x) = \frac{1}{2}\delta\sqrt{2}$.

In the circular part we have, with $u\mathbf{e}_r + v\mathbf{e}_\theta$ the displacement vector,

$$t_{rr} = E_C \frac{\partial u}{\partial r}, \quad t_{\theta\theta} = E_L\Big(\frac{1}{r}\frac{\partial v}{\partial \theta} + \frac{1}{r}u\Big), \quad t_{r\theta} = G\Big(\frac{\partial v}{\partial r} + \frac{1}{r}\frac{\partial u}{\partial \theta} - \frac{1}{r}v\Big). \tag{36}$$

Boundary conditions will be

$$\begin{array}{lllll} \text{at} & r & = & R: & u = v = 0 \quad \text{(no slip)} \\ \text{at} & r & = & R_a: & u = -\sum W_n \cos(n\theta), \quad v = \sum Z_n \sin(n\theta), \end{array}$$

where use is made of the symmetry at $\theta = 0$. A suitable first choice seems to be a simple displacement $u = -\delta\cos\theta$, $v = \delta\sin\theta$.

The two regimes are connected at $x = 0$, $\theta = -\theta_1$ by conditions of continuity: $u = \eta$, and $v = -\xi$.

Because of equilibrium $\mathcal{T}$ must satisfy

$$\nabla \cdot \mathcal{T} = \mathit{\Lambda}, \tag{37}$$

in both regions. If we introduce the dimensionless, small, parameters

$$\varepsilon = \frac{E_C}{E_L}, \qquad \gamma = \frac{G}{E_L}, \qquad \text{such that} \quad 2\gamma < \varepsilon \ll 1,$$

and substitute into (37) we find the equations

$$\xi_{xx} + \gamma(\xi_{yy} + \eta_{xy}) = 0, \tag{38a}$$

$$\gamma(\xi_{xy} + \eta_{xx}) + \varepsilon\eta_{yy} = 0, \tag{38b}$$

and

$$\varepsilon u_{rr} + \frac{\varepsilon}{r}u_r - \frac{1}{r^2}u + \frac{\gamma}{r^2}u_{\theta\theta} - \frac{1}{r^2}(1+\gamma)v_\theta + \frac{\gamma}{r}v_{r\theta} = 0 \tag{39a}$$

$$\frac{\gamma}{r}u_{r\theta} + \frac{1}{r^2}(1+\gamma)u_\theta + \frac{1}{r^2}v_{\theta\theta} + \gamma v_{rr} + \frac{\gamma}{r}v_r - \frac{\gamma}{r^2}v = 0 \tag{39b}$$

where subscripts denote a partial derivative.

By expanding ξ and η in a Fourier series in y

$$\xi(x,y) = \sum_{n=1}^{\infty} X_n(x)\sin(ny/a), \qquad \eta(x,y) = \sum_{n=1}^{\infty} Y_n(x)\cos(ny/a), \tag{40}$$

we arrive at

$$X_n'' - n^2\gamma X_n - \gamma n Y_n' = 0 \tag{41a}$$
$$\gamma n(X_n' + Y_n'') - n^2\varepsilon Y_n = 0 \tag{41b}$$

with solutions, decaying for $x \to \infty$, given by

$$X_n(r) = \sum_{j=1}^{2} A_j \, \mathrm{e}^{\lambda_j x}, \qquad Y_n(r) = \sum_{j=1}^{2} B_j \, \mathrm{e}^{\lambda_j x} \tag{42}$$

where

$$(\lambda_j^2 - n^2\gamma)A_j = \gamma n \lambda_j B_j$$

and $\lambda_{1,2}$ are the two solutions with *negative* real part of

$$\gamma\lambda^4 - (n\epsilon + \gamma^2 n(n-1))\lambda^2 + n^3\gamma^2 = 0.$$

By expanding u and v in a Fourier series in θ

$$u(r,\theta) = \sum_{n=0}^{\infty} U_n(r)\cos(n\theta), \qquad v(r,\theta) = \sum_{n=1}^{\infty} V_n(r)\sin(n\theta), \tag{43}$$

we arrive at

$$\varepsilon U_n'' + \frac{\varepsilon}{r}U_n' - \frac{1}{r^2}(1+n^2\gamma)U_n + \frac{n\gamma}{r}V_n' - \frac{n}{r^2}(1+\gamma)V_n = 0 \tag{44a}$$
$$\gamma V_n'' + \frac{\gamma}{r}V_n' - \frac{1}{r^2}(n^2+\gamma)V_n - \frac{n\gamma}{r}U_n' - \frac{n}{r^2}(1+\gamma)U_n = 0 \tag{44b}$$

which has the (explicit) solution:

if $n > 1$

$$U_n(r) = \sum_{j=1}^{4} C_j r^{\lambda_j}, \qquad V_n(r) = \sum_{j=1}^{4} D_j r^{\lambda_j} \tag{45a}$$

where

$$D_j = \frac{(1+\gamma+\lambda_j\gamma)(1-\varepsilon\lambda_j^2)}{n(n^2\gamma - 2\gamma - 1)}C_j,$$
$$\varepsilon\gamma\lambda^4 - (\varepsilon\gamma + \gamma + \varepsilon n^2)\lambda^2 + \gamma(n^2-1)^2 = 0;$$

if $n = 0$

$$U_0(r) = C_1 r^{\lambda} + C_2 r^{-\lambda}, \qquad \text{where} \quad \lambda = \sqrt{\frac{1}{\varepsilon}}; \tag{45b}$$

and if $n = 1$

$$U_1(r) = C_1 + C_2\log\Big(\frac{r}{R}\Big) + C_3\Big(\frac{r}{R_a}\Big)^{\lambda} + C_4\Big(\frac{r}{R}\Big)^{-\lambda},$$
$$V_1(r) = D_1 + D_2\log\Big(\frac{r}{R}\Big) + D_3\Big(\frac{r}{R_a}\Big)^{\lambda} + D_4\Big(\frac{r}{R}\Big)^{-\lambda}, \tag{45c}$$

where $\lambda = \Big(1 + \frac{1}{\varepsilon} + \frac{1}{\gamma}\Big)^{1/2}$ and

$$(1+\gamma)(D_1+C_1) = -\gamma C_2, \quad D_2 = -C_2,$$

$$\gamma D_3 = \varepsilon(1+\gamma+\lambda\gamma)C_3, \quad \gamma D_4 = \varepsilon(1+\gamma-\lambda\gamma)C_4.$$

An example of a very simple shape, with just $u(R_a) = -\delta\cos\theta$ and $v(R_a) = \delta\sin\theta$ such that we have only the n=1-term, is given in figure 9. The parameters are not chosen from any measurement, but hopefully not too unrealistically: $\varepsilon = 0.03$, $\gamma = 0.01$, $R = 10$, $R_a = 20$, and $\delta = 1$.

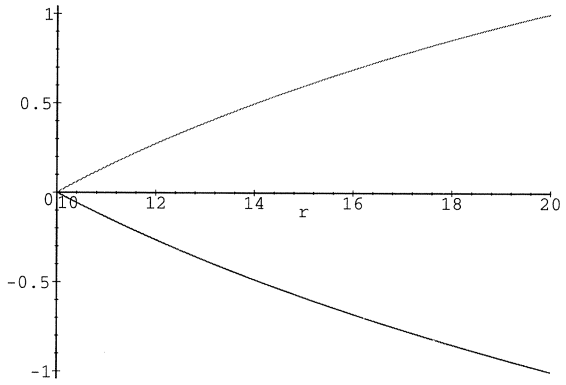

FIGURE 9. $U_1(r)$ and $V_1(r)$ for $10 \le r \le 20$.

A detail of interest is the following boundary layer behaviour. Since ε and γ are small, λ is invariably a large parameter. Consider for example the n=1 -term. Since variable r is always between R and R_a, the term $(r/R)^{-\lambda}$ is practically absent everywhere, except near $r = R$. The same is true for $(r/R_a)^{\lambda}$ near $r = R_a$. This suggests strong gradients in displacement just below the surface of the material, which might well be responsible for residual stresses and hence an uneven surface, maybe even blister formation or cracks in the surface.

This is evidently the result of the relatively low resistance against shear. Any shearing force applied at the surface results into a deformation of the material only near the surface.

Further results are possible only after acquisition of numerical values of the various problem parameters, and the programming and numerical evaluation of the present solution.

5. Relevant literature

The problems described by Trespa have parallels in other industrial processes and, while there was no time to investigate all the areas, it is worth pointing out the relevant literature.

The cracks which appear in the finished product do not occur during the viscous stage and so must occur when the material is hot. In which case it is possible that the cracks appear due to the residual stress calculated in §4 or temperature effects. If temperature variation is the culprit it is well known that thermal stress is proportional to temperature gradient and there are numerous texts on elasticity which describe this [4, 5].

Blistering is a problem frequently encountered in the paint industry and for a similar reason as in the present problem. The paint layer forms a skin which prevents entrapped gas from escaping and so a bubble or blister forms under the skin. A good survey on such problems may be found in [6].

Flow through a porous media, such as paper, has been mentioned already [1]. This work was related to the production of formica. Further information on lubrication flow into a porous media may be found in [2].

REFERENCES

1. TAYLER A.B., Fluid flow between a roller and absorbent compressible paper. *Q. Jl. Mech.Appl. Math* **31**(4) pp. 481-495, 1978.
2. CAMERON A., *Basic lubrication theory*, 3rd edition, pp. 143-144. Ellis Horwood 1981.
3. LANGLOIS W.E., *Slow viscous flow*, chapter IX. MacMillan 1964.
4. LOVE A.E.H., *A treatise on the mathematical theory of elasticity.* Dover 1944.
5. LANDAU L.D. & LIFSHITZ E.M., *Theory of elasticity.* Pergammon 1986.
6. KORNUM L.O. & NIELSEN H.K.R., *Surface defects in drying paint films. Prog. in Org. Coatings* 8 pp. 275–324, 1980.
7. BOWEN R.M., Theory of mixtures, *Continuum Physics* **3**, A. CEMAL ERINGEN (eds.), Academic Press. New York 1976.
8. SOKOLNIKOFF I.S., *Mathematical theory of elasticity*, McGraw-Hill, New York 1956.

33rd European Study Group with Industry
14 — 18 September 1998

pp. 55 – 61

Detection of Metastases in Human Lungs from CT-Scans

Jan Schreuder, Barbera van de Fliert
Universiteit Twente, Fac Toegepaste Wiskunde
P.O. Box 217, 7500 AE Enschede, The Netherlands

Jaap Molenaar
Technische Universiteit Eindhoven, DepartmentW&I, IWDE
P.O. Box 513, 5600 MB Eindhoven, The Netherlands

One of the possibilities to assist physicians with their diagnostic work based on CT-scans would be a tool for automatic detection of metastases in human lungs. The present project stems from the 'Dr. Daniel den Hoedkliniek' in Rotterdam. The problem was successfully tackled during the week and resulted in a highly efficient algorithm to detect metastases from CT-data. The algorithm is restricted to metastases that are not attached to each other or to the lung edges. A first attempt to implement it into a Fortran program yielded successful results on artificial data sets. For fine-tuning of parameters the algorithm should be applied to real data from the clinic.

1. Introduction

One of the problems presented during the Study Group in Leiden, September 1998, concerned the automatic detection of possible metastases - i.e. clusters of tumor cells - in human lungs. These metastases are approximately spherical with diameters in the range 0.3-2 cm. A computer assisted diagnostic program should be able to identify these objects efficiently.

The lungs often serve as initial 'target organ' for tumors with venous drainage primarily to this organ. The entire output of the right side of the heart as well as virtually all lymphatic fluids produced by body tissues flows through the pulmonary vascular system. Therefore it is not surprising that metastases to the lungs are quite common. Patients with tumors that initially arise in the lungs are at high risk of developing pulmonary metastases early. If left untreated such metastases may be a primary cause of death.

In the seventies computers were introduced in X-ray diagnostics. They had an enormous impact on the field of röntgenology. New measuring and imaging methods became available, which gave the field a new impetus. One of the main improvements was the possibility of transaxial scanning of patients. Until then tomography produced only longitudinal scans.

Nowadays the spiral volumetric CT technique has introduced truly contiguous scanning which is independent of e.g. breathing. Subsequent serial-section axial images are generated by means of filtered back projection after interpolation.

Earlier research by students of Prof. M. Keane, see [Ber94] and [Sch95], showed that the route starting from random lung shapes, edge/contour detection, in order to come to detection of metastases was not quite feasible. With the Study Group we attempted a direct approach which has the advantage of being very efficient since the grid points of a CT-scan are visited only once.

2. PROBLEM

At the Study Group Dr.M. Oudkerk of the Dr. Daniel den Hoedkliniek, a medical center for cancer treatment in Rotterdam, presented a problem, which - reduced to its essence - reads as:

'When making a diagnosis by using a CT scan, one looks for spherical shapes amidst bones and lung tissue. Where the bones show a value of 1000 in an appropriate system of units on the CT scan and long tissue are at 0, the spheres distinguish themselves at a value of around 150. For the automatic pattern recognition one can assume that the spheres are unconnected from each other and the lung edges, with unknown diameter and position'.

The present way of scanning the data makes use of the presentation of the grey value pattern in a horizontal slice on a screen. Here `horizontal' is meant with respect to the patient in an upright position. In fact, no 3-D but only 2-D representations are used. The sophisticated interface allows the user to scroll through adjacent horizontal slices in a fast and convenient way. If a suspicious 2-D object is observed in one slice, the inspector may immediately deduce from the pictures of the slices directly above and below the slice under consideration whether the object is part of a 3-D spherical object or that it is connected to, e.g., a vein image. The expert knowledge comprises a lot of experience about the objects that can be expected to be present in specific regions of the lung. Although the lungs of different people may differ considerably, the human eye is highly capable in detecting irregular patterns.

However, the present detection method of visual inspection is not yet perfect. Clinical studies in the use of chest radiographs for the detection of lung metastases have demonstrated that even highly skilled and highly motivated radiologists, task directed to detect any finding of suspicion for metastases, and working with high quality chest radiographs, still fail to detect more than 30% of lung cancers that can be detected retrospectively [LLF98]. So, a computer tool pointing out suspicious cells or giving a clearance could be an enormous help in saving valuable time to the physicians.

In the Dr. Daniel den Hoedkliniek screening of the lungs using computer tomography is conducted on a daily basis. This screening serves for the detection of

pulmonary metastases. The head of the radiology section would like to dispose of a mathematical model of the lungs and the process of an optimal scanning protocol.

It was explicitly mentioned to focus the project on spherical metastases that are not attached to the lung boundaries or the heart. The metastases may be easily distinguished from areas filled with air, water, or bones. More problems are to be expected with discriminating metastases from lung and heart tissues and veins.

3. DATA

In a CT scan a 6 – 8 mm spiral slice of the patient is made. This raw data is first translated into about 60 – 100 horizontal slices, flat and equidistant. The available data are 512x512 grid points per horizontal slice ($\Delta x = \Delta y \geq 0.5$mm), 60 – 100 times ($\Delta z \geq 1.5$mm). Values, called Hounsfield Units (grey value), range from – 1000 (air) over 0 (water) to 1000 (bone). Lung and heart tissues, veins, and metastases have values in the range of about 40 – 150.

4. APPROACH

There are many possible approaches to detect discs represented by grid points in two dimensions. The important issue is to do this as accurate and as fast as possible. In view of the enormous number of points to be considered it is important to visit each point preferably only once.

As a first step we simplify the problem such that to each grid point the value 1 is assigned if the Hounsfield filter value of the CT scan is between 40 and 150 (the range in which metastases data are known to fall), and the value 0 otherwise. Suspicious objects thus correspond to connected areas of neighboring grid points labeled with a one. Positions are considered to be neighbors if they are in contact horizontally or vertically; diagonal neighbors are not included, although this definition could be relaxed easily. The second step is looking for discs in 2-D, and eventually for spheres in 3-D. The Study Group only discussed the application of sieves for detection of discs in 2-D slices, realizing that extension to 3-D sieves will be relatively straightforward.

In 2-D the problem is to determine whether a set of identified neighboring pixels in a rectangular grid is more or less 'disc-like'. The following ideas were proposed and discussed:

1. Spotlight approach.

Construct predefined discs, $B_1, \ldots, B_M$, of sets of grid points which are considered to represent discs on a rectangular grid. The object S is compared to the predefined discs that have nearly the same number of pixels as the still unidentified object. As a measure of similarity between the objects the number of grid points that both objects have in common, could be taken. This measure could be referred to as the 'Hamming distance'. A selection criterion then could be

$$\frac{d(S,B_i)}{N} \leq \varepsilon_i \quad , \qquad i = 1, \ldots, M$$

with *d(S1,S2)* the 'Hamming'-distance and *N* the number of pixels of *S*. Reliable values for the parameters ε_i should be fitted from analyzing real data sets.

2. *Borderline search.*
From computer graphics it is known that efficient techniques are available to determine the borderline of the 2-D object once one point of the object is indicated. This borderline should be compared to a circle. An appropriate measure for this comparison could be found following the previous idea in 1 .

3. *Paint filling approach.*
From computer graphics efficient techniques are available to find an object indicated by neighboring 'ones' in a data file if only one point of the object is indicated. The painted area should be compared to a disc. It should be simple to find an appropriate measure for this comparison, in the same spirit as for methods 1 and 2.

4. *Hemker approach.*
We eventually decided to use a method suggested by Hemker. The idea is as follows. The data points (containing zeros and ones) are visited in a systematic way: the matrix is searched by columns, top down, starting left. The first position containing a one is assigned the label 'a'. The next position containing a one is initially assigned the label 'b'. However, if this position is neighboring to a position with label 'a', the position under consideration gets the label 'a' instead of 'b'. The next position containing a one and not being a neighbor of a position with label 'a' or 'b' gets the label 'c'. Etcetera. If at some moment in the labeling process it turns out that two positions with different labels are neighboring, it is administrated that these objects, which until that time have been considered as being separated, are part of one and the same object. This is done by identifying the labels accordingly. From then on both objects are treated as one object. An example of the labeling and identification procedure is as follows:

labeling of 'ones'			
0	1 ***b***	0	0
1 ***a***	1 ***a=b***	1 ***a=b***	0
1 ***a***	0	0	0
0	1 ***c***	1 ***c***	0

Identification label		
a ***b*** ***c*** ***d*** . .	⇒	***a*** ***a*** ***c*** ***d*** . .

Per object (or label) the following properties are calculated: the total number of grid points N and the quantities $\sum_i x_i$, $\sum_i y_i$, $\sum_i x_i^2$, $\sum_i y_i^2$, where x_i and y_i are the 2-D coordinates of the grid points. The method has the advantage that each point in the data matrix is visited only once. That is because these quantities, being simple sums over the members of an object, can be updated as soon as a new point is assigned to a label.

After the matrix has been searched through, the information gathered per object allows for the calculation of the inertia tensor ***I*** of the 2-D object with *N* points:

$$I = \begin{bmatrix} I_{xx} & I_{xy} \\ I_{yx} & I_{yy} \end{bmatrix},$$

with

$$I_{xx} = (\tfrac{1}{N}\sum_1^N y_i^2) - \bar{y}^2, \quad \bar{y} = \tfrac{1}{N}\sum_1^N y_i, \quad I_{xy} = I_{yx} = \bar{x}\bar{y} - \tfrac{1}{N}\sum_1^N x_i y_i,$$

and I_{yy} defined in an analogous manner. The eigenvalues I_1 and I_2 of $\boldsymbol{I}$ are the principal moments of inertia of the object. For a uniform disc the inertia tensor is diagonal and $I_1 = I_2$.

These moments are to be compared to the principal moments of inertia of a disc of nearly the same size. The radius of such a disc can be deduced from the number N of grid points per object, since the area per grid point is known.

Although these ideas are quite simple, inaccuracy comes in via the discretization: even a perfect disc is represented in the data by a finite number of points and the shape of this collection depends on the relative positions of disc and grid points. The smaller the disc, the fewer the number of representing points and thus the bigger the inaccuracy will be. This inaccuracy has been estimated as a function of disc size. To that end some simulations have been performed. The procedure used was as follows:

- Position a disc of prescribed radius R randomly in the plane.
- Compute its pixel discretization.
- Compute N, the number of pixels covered by the disc.
- Compute I_1 and I_2 of the discretized disc; they depend on R, N, and the geometry.
- Compare these moments with the moments of inertia $I_1 = I_2 = I_d$ of the original disc by calculating

$$\varepsilon(R,N) = \frac{(I_1(R,N) - I_d(R)) + (I_2(R,N) - I_d(R)}{I_d(R)}.$$

The results of the simulations are used as follows. Given a 'disc-like' set of N pixels, a family of discs exists which all have this set as discretized representation. Of this family the smallest and the biggest discs are found with radii $R_{\min}$ and $R_{\max}$. For these the deviations $\varepsilon^- = \varepsilon(R_{\min}, N)$ and $\varepsilon^+ = \varepsilon(R_{\max}, N)$ are calculated. For the biggest disc the difference is positive, whereas for the smallest disc it is negative. In the table below the averages of ε^- and ε^+ are given as functions of the number N of pixels in a number of classes.

N	$\varepsilon^-(N)$	$\varepsilon^+(N)$
1–2	–1	+1.5
3–12	–0.4	+0.7
13–28	–0.2	+0.35
29–50	–0.15	+0.25
51–82	–0.12	+0.15
83–108	–0.06	+0.10

This table can be used as a sieve to decide whether a detected discretized object of N points is likely to represent a disc.

5. RESULTS AND CONCLUSIONS

During the week we developed a computer program for the analysis of 2-D data via the Hemker approach. In these data files artificial disc-like objects were added at random. The results showed that disc-like objects could be detected without any problem. The chance to detect an object depends on its shape. Using ranges in the table given above, we could only detect 'nearly-discs'. In CT-Scan practice the objects may be quite far from disc-shaped (or spheres in 3-D), so that fine-tuning of the parameters in the sieve is necessary. Reliable values of the parameters to be used in analyzing real data should be obtained with use of expert experience and from analysis of a great number of scans.

Later the method was extended to 3-D but this is straightforward, since the present approach does not contain any element specific for 2-D. Computing times appeared to be very short. The search procedures could be implemented even in a more efficient way than sketched above. Extension to 3-D data did not cause any trouble in this respect, even for real data sets that contain as much as 10 million data points per scan.

It should be emphasised that the approach outlined above is only applicable in case of metastases that are not attached to each other, the lung edges or the heart. In those cases more sophisticated methods of pattern recognition are necessary.

ACKNOWLEDGEMENT

The first author wishes to thank Drs. J.G. Heeres, radiodiagnost of the Enschede hospital MST, for his explanations of the medical aspects of the problem.
During the workshop contributions were obtained from Pieter Roos (Universiteit Twente), Erik Fledderus (KPN Research), Piet Hemker (Cenbtrum voor Wiskunde en Informatica), Bob Planque (Universiteit Leiden), Damien White (Universiteit Utrecht).

REFERENCES

[Ber94] BERG, ERIC VAN DEN, *A random model for the shape of the human lung*, Master's Thesis Delft University of Technology (May, 1994).

[FHP96] FLIERT, B.W. VAN DE, HULSHOF, J., PELETIER, L.A. , SCHOTTING, R., *Partial differential equations practical*, Mathematical Institute, Leiden University, 1996.

[LLF98] LO, SHIH-CHUNG B., LIN, JYH-SHYAN J., FREEDMAN, MATTHEW T., MUN, SEONG K., Application of Artificial Neural Networks to Medical Image Pattern Recognition: Detection of Clustered Microcalcifications on Mammograms and Lung Cancer on Chest Radiographs, *Journal of VSLI Signal Processing* **18** (1998), 263–274.

[Oud98] OUDKERK, M. *Pattern recognition in CT scans*, Presentation at the Study Group '98, Afd Radiologie, Dr Daniel Den Hoed Kliniek, Rotterdam, tel 010 4391484, fax 010 4391007.

[Sch95] SCHOUTEN, BARRY, *Images and Random Quadtrees*, Master's Thesis Delft University of Technology (July, 1995).

33rd European Study Group with Industry
14 – 18 September 1998

pp. 63 – 67

Stability of Stationary Velocity Profiles in Fiber Spinning

C.J. van Duijn
CWI, Amsterdam & Delft Technical University, Department of Mathematics,

J. Hulshof
Mathematical Institute, University of Leiden,

R. van der Hout
Akzo Nobel Central Research, Arnhem & Mathematical Institute, University of Leiden,

J.H. Smink
Akzo Nobel Central Research, Arnhem

1. The problem

We consider a process of fiber spinning, where a viscous (but not necessarily Newtonian) fluid is being pushed through a narrow "spinning hole" and, upon exit, is being stretched, the latter step in order to obtain an acceptable alignment of the (polymeric) molecules in the fluid. This alignment is necessary for the final mechanical properties of the fiber. After leaving the spinning hole, the fluid passes through a layer of air (the "air gap") and enters a bath, in which it solidifies almost instantaneously. Somewhere inside this bath, the fiber is being drawn by a wheel, which delivers the force, necessary for the stretching process.
When the speed of the drawing wheel is set to high, it is impossible to obtain a uniform fiber: one clearly observes variations in the fiber diameter. This phenomenon is called *draw resonance*. Experimental evidence suggests that the *draw ratio*, that is, the ratio between the speeds at the wheel and at the exit of the spinning hole, is the unique parameter to steer the onset of draw resonance, and for Newtonian fluids this is known to be true. The reader is referred to [1] and [2]. In the Newtonian case, the onset of draw resonance can be shown to be a Hopf bifurcation.

The question, asked to the Study Group, was to extend the results on Newtonian fluids to fluids with more general rheologies, with power law fluids as a first choice. What came out of the Study Group was not yet a final solution to this problem, but rather an attempt to come to an easier formulation of the model equations. At the workshop, we thought that we had succeeded, but afterwards we found that there was a hidden mistake, which we could not easily correct. This mistake in itself is worth mentioning, because the approach we tried may be successful in other cases, and this mistake may easily slip into the considerations there. In this note, we restrict ourselves to the Newtonian case, because it is easy to describe the mistake in this setting, and the power law setting would not add anything.

As a final remark, we note that the "power law case" has been solved now, by using similar methods as we did in the Newtonian case. A publication is in preparation.

Apart from the authors, during the study group the following persons have worked on this problem: Pieter de Groen (Free University, Bruxelles) and Sandro Merino (University of Strathclyde, Glasgow).

2. Summary of the previous results

When the (very thin) fluid jet is considered one dimensional, a nondimensionalized model for the Newtonian case is given by

$$\rho_\tau + (\rho v)_x = 0 \tag{1}$$
$$Re(\rho v_\tau + \rho v v_x) = (\rho v_x)_x \tag{2}$$
$$\rho(0,\tau) = v(0,\tau) = 1 \tag{3}$$
$$v(1,\tau) = s, \tag{4}$$

where τ, x, ρ and v are nondimensionalized time, length along the jet, cross-section and speed, respectively. The parameter s is the draw ratio. Re is the Reynolds number, defined by $Re = \frac{v_s \ell \rho}{\eta}$, where v_s, ℓ, ρ and η are, respectively, the speed at the exit of the spinning hole, the length of the air gap, the density and the (Trouton) viscosity. Actually, Re is very small, so that we are left with

$$(P_1)\begin{cases} \rho_\tau + (\rho v)_x = 0 \\ v_{xx} + \frac{\rho_x v_x}{\rho} = 0 \\ \rho(0,\tau) = v(0,\tau) = 1 \\ v(1,\tau) = s \\ \rho(x,0) = \hat{\rho}(x), \end{cases}$$

where $\hat{\rho}$ is an initial situation. Note that (P_1) has a unique stationary solution, given by $\rho(x,t) = \rho_0(x) = s^{-x}$, $v(x,t) = v_0(x) = s^x$, where we have assumed that $\hat{\rho} = \rho_0$. We are interested in the *stability* of this stationary solution. Therefore, we linearize around ρ_0, v_0, as follows: we set

$$\rho = s^{-x}(1 + p(x,\tau)); \quad v = s^x(1 + q(x,\tau)),$$

and we omit all terms that are of order > 1 in $\{p, q\}$. Next, we require that the boundary condition are not perturbed: $p(0,\tau) = q(0,\tau) = q(1,\tau) = 0$. The resulting system of equations for $\{p, q\}$ can be transformed into one single equation

$$\sigma(\tau) = \frac{s \log s}{s-1} \int_0^{(s-1)/(s \log s)} \left\{ \frac{ys \log s + 1 - s}{s(1 - y \log s)^2} \right\} \sigma(\tau - y)\, dy, \tag{5}$$

where $\sigma(\tau)$ is the perturbation in drawing force. The next step is to show that the stability question is completely determined by the complex valued eigenvalues λ, given by

$$\frac{s \log s}{s-1} \int_0^{(s-1)/(s \log s)} \left\{ \frac{ys \log s + 1 - s}{s(1 - y \log s)^2} \right\} e^{-\lambda y}\, dy = 1.$$

The stationary solutions are unstable when there is an eigenvalue with positive real part, and stable when all eigenvalues are in the left half plane. A proof is contained in [3, Section I, Th.5.4].

3. Approach of the Study Group

The first purpose has been to come to a different problem formulation, which we did for the Newtonian case first. We did not a priori assume Re to be small, but we have used the letter ε in stead of Re.

We introduce the new coordinates

$$\psi(x, \tau) = \int_0^x \rho(\xi, \tau)\, d\xi, \qquad t(x, \tau) = \tau.$$

This choice is justified by the fact that $\psi_x = \rho > 0$. Note that ψ is a stream function and that

$$\psi_\tau = 1 - \rho v.$$

By abuse of notation, we use the same letters for the dependent variables as before. Upon the transformation, the region $\{0 < x < 1\}$ is transformed into the region

$$0 < \psi < \int_0^1 \rho(\xi, t)\, d\xi = \zeta(t),$$

where

$$\zeta'(t) = 1 - \rho(\zeta(t), t)s.$$

Apparently, the coordinate transformation has left us with a free boundary problem. Note that, in the stationary case, we have that $\rho(\zeta(t), t) = \frac{1}{v(\zeta(t), t)} = \frac{1}{s}$, so that $\zeta'(t) = 0$, as expected.

In the new coordinates, the differential equations read

$$\rho_t + \rho_\psi + \rho^2 v_\psi = 0, \tag{6}$$

$$v_t + v_\psi = \frac{1}{\varepsilon}(\rho^2 v_\psi)_\psi. \tag{7}$$

The equations are valid in the region $0 < \psi < \zeta(t)$, where $\zeta'(t) = 1 - \rho(\zeta(t), t)s$. As boundary conditions we have

$$\rho = v = 1 \qquad (\psi = 0), \tag{8}$$

$$v = s \qquad (\psi = \zeta(t)). \tag{9}$$

The stationary solution $\{\rho_0, v_0\}$ satisfies

$$\rho_0' + \rho_0^2 v_0' = 0, \tag{10}$$

$$\varepsilon v_0' = \left(\frac{v_o'}{v_0^2}\right)'. \tag{11}$$

By (8), we find from (10) that

$$v_0 \rho_0 = 1. \tag{12}$$

Equation (11) may be integrated, to yield that

$$\varepsilon v_0 = \frac{v_0'}{v_0^2} - c. \tag{13}$$

From this result we deduce that

$$\int_1^s \frac{dv}{v^2(\varepsilon v + c)} = \zeta_0. \tag{14}$$

In order to determine c, we recall that, in the "old" variables, we have

$$\frac{d\psi}{dx} = \rho_0 = \frac{1}{v_0},$$

so that

$$1 = \int_0^1 v_0 \frac{d\psi}{dx}\, dx = \int_0^{\zeta_0} v_0\, d\psi.$$

From (13) we deduce that $d\psi = \frac{dv_0}{v_0^2(\varepsilon v_0 + c)}$, so that

$$\int_1^s \frac{dv}{v(\varepsilon v + c)} = 1. \tag{15}$$

This relation enables us to determine c and, thus, v_0 and ρ_0.

So far so good. In order to analyze the stabilty of the steady solution, we linearise around (6), (7), writing

$$\rho = \rho_0 + u; \qquad v = v_0 + w.$$

Formally, this gives, to first order,

$$u_t + u_\psi + 2\rho_0 u v_0' + \rho_0^2 w_\psi = 0,$$

$$w_t + w_\psi = \frac{1}{\varepsilon}(2\rho_0 u v_0' + \rho_0^2 w_\psi)_\psi.$$

But here we made the following mistake. When we perturb ρ, we implicitly perturb our coordinate ψ, which must be taken into account in the linearization. We did not perceive this during the workshop, and afterwards we found that correcting the mistake made the equations rather awful.
After the workshop and the detection of the mistake, we again tried the "old" approach on power law fluids. We seem to have been successful now, and another publication is in preparation.

REFERENCES

1. MATOVICH, M.A. & J.R.A. PEARSON, Eng.Chem. Fundamentals 8, 512 (1969)
2. PEARSON, J.R.A & MATOVICH, M.A., Eng. CHem. Fund. 8, 605 (1969)
3. DIEKMANN, O., S.A. VAN GILS, S.M. VERDUYN LUNEL & H.-O.WALTHER, *Delay Equations*, Springer, 1995.

CWI SYLLABI

1 Vacantiecursus 1984: *Hewet - plus wiskunde.* 1984.

2 E.M. de Jager, H.G.J. Pijls (eds.). *Proceedings Seminar 1981–1982. Mathematical structures in field theories.* 1984.

3 W.C.M. Kallenberg, et al. *Testing statistical hypotheses: worked solutions.* 1984.

4 J.G. Verwer (ed.). *Colloquium topics in applied numerical analysis, volume 1.* 1984.

5 J.G. Verwer (ed.). *Colloquium topics in applied numerical analysis, volume 2.* 1984.

6 P.J.M. Bongaarts, J.N. Buur, E.A. de Kerf, R. Martini, H.G.J. Pijls, J.W. de Roever. *Proceedings Seminar 1982–1983. Mathematical structures in field theories.* 1985.

7 Vacantiecurus 1985: *Variatierekening.* 1985.

8 G.M. Tuynman. *Proceedings Seminar 1983–1985. Mathematical structures in field theories, Vol.1 Geometric quantization.* 1985.

9 J. van Leeuwen, J.K. Lenstra (eds.). *Parallel computers and computations.* 1985.

10 Vacantiecursus 1986: *Matrices.* 1986.

11 P.W.H. Lemmens. *Discrete wiskunde: tellen, grafen, spelen en codes.* 1986.

12 J. van de Lune. *An introduction to Tauberian theory: from Tauber to Wiener.* 1986.

13 G.M. Tuynman, M.J. Bergvelt, A.P.E. ten Kroode. *Proceedings Seminar 1983–1985. Mathematical structures in field theories, Vol.2.* 1987.

14 Vacantiecursus 1987: *De personal computer en de wiskunde op school.* 1987.

15 Vacantiecursus 1983: *Complexe getallen.* 1987.

16 P.J.M. Bongaarts, E.A. de Kerf, P.H.M. Kersten. *Proceedings Seminar 1984–1986. Mathematical structures in field theories, Vol.1.* 1988.

17 F. den Hollander, H. Maassen (eds.). *Mark Kac seminar on probability and physics. Syllabus 1985–1987.* 1988.

18 Vacantiecursus 1988. *Differentierekening.* 1988.

19 R. de Bruin, C.G. van der Laan, J. Luyten, H.F. Vogt. *Publiceren met LATEX.* 1988.

20 R. van der Horst, R.D. Gill (eds.). *STATAL: statistical procedures in Algol 60, part 1.* 1988.

21 R. van der Horst, R.D. Gill (eds.). *STATAL: statistical procedures in Algol 60, part 2.* 1988.

22 R. van der Horst, R.D. Gill (eds.). *STATAL: statistical procedures in Algol 60, part 3.* 1988.

23 J. van Mill, G.Y. Nieuwland (eds.). *Proceedings van het symposium wiskunde en de computer.* 1989.

24 P.W.H. Lemmens (red.). *Bewijzen in de wiskunde.* 1989.

25 Vacantiecursus 1989: *Wiskunde in de Gouden Eeuw.* 1989.

26 G.G.A. Bäuerle et al. *Proceedings Seminar 1986–1987. Mathematical structures in field theories.* 1990.

27 Vacantiecursus 1990: *Getallentheorie en haar toepassingen.* 1990.

28 Vacantiecursus 1991: *Meetkundige structuren.* 1991.

29 A.G. van Asch, F. van der Blij. *Hoeken en hun Maat.* 1992.

30 M.J. Bergvelt, A.P.E. ten Kroode. *Proceedings seminar 1986–1987. Lectures on Kac-Moody algebras.* 1992.

31 Vacantiecursus 1992: *Systeemtheorie.* 1992.

32 F. den Hollander, H. Maassen (eds.). *Mark Kac seminar on probability and physics. Syllabus 1987–1992.* 1992.

33 P.W.H. Lemmens (ed.). *Meetkunde van kunst tot kunde, vroeger en nu.* 1993.

34 J.H. Kruizinga. *Toegepaste wiskunde op een PC.* 1992.

35 Vacantiecursus 1993: *Het reële getal.* 1993.

36 Vacantiecursus 1994: *Computeralgebra.* 1994.

37 G. Alberts. *Wiskunde en praktijk in historisch perspectief. Syllabus.* 1994.

38 G. Alberts, J. Schut (eds.). *Wiskunde en praktijk in historisch perspectief. Reader.* 1994.

39 E.A. de Kerf, H.G.J. Pijls (eds.). *Proceedings Seminar 1989–1990. Mathematical structures in field theory.* 1996.

40 Vacantiecursus 1995: *Kegelsneden en kwadratische vormen.* 1995.

41 Vacantiecursus 1996: *Chaos.* 1996.

42 H.C. Doets. *Wijzer in Wiskunde.* 1996.

43 Vacantiecursus 1997: *Rekenen op het Toeval.* 1997.

44 Vacantiecursus 1998: *Meetkunde, Oud en Nieuw.* 1998.

45 Vacantiecursus 1999: *Onbewezen Vermoedens.* 1999.

46 P.W. Hemker, B.W. van de Fliert (eds.). *Proceedings of the 33^{rd} European Study Group with Industry.* 1999.

47 K.H. Dzhaparidze. *Introduction to Option Pricing in a Securities Market.* 1999.

MC SYLLABI

1.1 F. Göbel, J. van de Lune. *Leergang besliskunde, deel 1: wiskundige basiskennis.* 1965.

1.2 J. Hemelrijk, J. Kriens. *Leergang besliskunde, deel 2: kansberekening.* 1965.

1.3 J. Hemelrijk, J. Kriens. *Leergang besliskunde, deel 3: statistiek.* 1966.

1.4 G. de Leve, W. Molenaar. *Leergang besliskunde, deel 4: Markovketens en wachttijden.* 1966.

1.5 J. Kriens, G. de Leve. *Leergang besliskunde, deel 5: inleiding tot de mathematische besliskunde.* 1966.

1.6a B. Dorhout, J. Kriens. *Leergang besliskunde, deel 6a: wiskundige programmering 1.* 1968.

1.6b B. Dorhout, J. Kriens, J.Th. van Lieshout. *Leergang besliskunde, deel 6b: wiskundige programmering 2.* 1977.

1.7a G. de Leve. *Leergang besliskunde, deel 7a: dynamische programmering 1.* 1968.

1.7b G. de Leve, H.C. Tijms. *Leergang besliskunde, deel 7b: dynamische programmering 2.* 1970.

1.7c G. de Leve, H.C. Tijms. *Leergang besliskunde, deel 7c: dynamische programmering 3.* 1971.

1.8 J. Kriens, F. Göbel, W. Molenaar. *Leergang besliskunde, deel 8: minimaxmethode, netwerkplanning, simulatie.* 1968.

2.1 G.J.R. Förch, P.J. van der Houwen, R.P. van de Riet. *Colloquium stabiliteit van differentieschema's, deel 1.* 1967.

2.2 L. Dekker, T.J. Dekker, P.J. van der Houwen, M.N. Spijker. *Colloquium stabiliteit van differentieschema's, deel 2.* 1968.

3.1 H.A. Lauwerier. *Randwaardeproblemen, deel 1.* 1967.

3.2 H.A. Lauwerier. *Randwaardeproblemen, deel 2.* 1968.

3.3 H.A. Lauwerier. *Randwaardeproblemen, deel 3.* 1968.

4 H.A. Lauwerier. *Representaties van groepen.* 1968.

5 J.H. van Lint, J.J. Seidel, P.C. Baayen. *Colloquium discrete wiskunde.* 1968.

6 K.K. Koksma. *Cursus ALGOL 60.* 1969.

7.1 *Colloquium moderne rekenmachines, deel 1.* 1969.

7.2 *Colloquium moderne rekenmachines, deel 2.* 1969.

8 H. Bavinck, J. Grasman. *Relaxatietrillingen.* 1969.

9.1 T.M.T. Coolen, G.J.R. Förch, E.M. de Jager, H.G.J. Pijls. *Colloquium elliptische differentiaalvergelijkingen, deel 1.* 1970.

9.2 W.P. van den Brink, T.M.T. Coolen, B. Dijkhuis, P.P.N. de Groen, P.J. van der Houwen, E.M. de Jager, N.M. Temme, R.J. de Vogelaere. *Colloquium elliptische differentiaalvergelijkingen, deel 2.* 1970.

10 J. Fabius, W.R. van Zwet. *Grondbegrippen van de waarschijnlijkheidsrekening.* 1970.

11 H. Bart, M.A. Kaashoek. H.G.J. Pijls, W.J. de Schipper, J. de Vries. *Colloquium halfalgebra's en positieve operatoren.* 1971.

12 T.J. Dekker. *Numerieke algebra.* 1971.

13 F.E.J. Kruseman Aretz. *Programmeren voor rekenautomaten; de MC ALGOL 60 vertaler voor de EL X8.* 1971.

14 H. Bavinck, W. Gautschi, G.M. Willems. *Colloquium approximatietheorie.* 1971.

15.1 T.J. Dekker, P.W. Hemker, P.J. van der Houwen. *Colloquium stijve differentiaalvergelijkingen, deel 1.* 1972.

15.2 P.A. Beentjes, K. Dekker, H.C. Hemker, S.P.N. van Kampen, G.M. Willems. *Colloquium stijve differentiaalvergelijkingen, deel 2.* 1973.

15.3 P.A. Beentjes, K. Dekker, P.W. Hemker, M. van Veldhuizen. *Colloquium stijve differentiaalvergelijkingen, deel 3.* 1975.

16.1 L. Geurts. *Cursus programmeren, deel 1: de elementen van het programmeren.* 1973.

16.2 L. Geurts. *Cursus programmeren, deel 2: de programmeertaal ALGOL 60.* 1973.

17.1 P.S. Stobbe. *Lineaire algebra, deel 1.* 1973.

17.2 P.S. Stobbe. *Lineaire algebra, deel 2.* 1973.

17.3 N.M. Temme. *Lineaire algebra, deel 3.* 1976.

18 F. van der Blij, H. Freudenthal, J.J. de Iongh, J.J. Seidel, A. van Wijngaarden. *Een kwart eeuw wiskunde 1946-1971, syllabus van de vakantiecursus 1971.* 1973.

19 A. Hordijk, R. Potharst, J.Th. Runnenburg. *Optimaal stoppen van Markovketens.* 1973.

20 T.M.T. Coolen, P.W. Hemker, P.J. van der Houwen, E. Slagt. *ALGOL 60 procedures voor begin- en randwaardeproblemen.* 1976.

21 J.W. de Bakker (red.). *Colloquium programmacorrectheid.* 1975.

22 R. Helmers, J. Oosterhoff, F.H. Ruymgaart, M.C.A. van Zuylen. *Asymptotische methoden in de toetsingstheorie; toepassingen van naburigheid.* 1976.

23.1 J.W. de Roever (red.). *Colloquium onderwerpen uit de biomathematica, deel 1.* 1976.

23.2 J.W. de Roever (red.). *Colloquium onderwerpen uit de biomathematica, deel 2.* 1977.

24.1 P.J. van der Houwen. *Numerieke integratie van differentiaalvergelijkingen, deel 1: eenstapsmethoden.* 1974.

25 *Colloquium structuur van programmeertalen.* 1976.

26.1 N.M. Temme (ed.). *Nonlinear analysis, volume 1.* 1976.

26.2 N.M. Temme (ed.). *Nonlinear analysis, volume 2.* 1976.

27 M. Bakker, P.W. Hemker, P.J. van der Houwen, S.J. Polak, M. van Veldhuizen. *Colloquium discretiseringsmethoden.* 1976.

28 O. Diekmann, N.M. Temme (eds.). *Nonlinear diffusion problems.* 1976.

29.1 J.C.P. Bus (red.). *Colloquium numerieke programmatuur, deel 1A, deel 1B.* 1976.

29.2 H.J.J. te Riele (red.). *Colloquium numerieke programmatuur, deel 2.* 1977.

30 J. Heering, P. Klint (red.). *Colloquium programmeeromgevingen.* 1983.

31 J.H. van Lint (red.). *Inleiding in de coderingstheorie.* 1976.

32 L. Geurts (red.). *Colloquium bedrijfsystemen.* 1976.

33 P.J. van der Houwen. *Berekening van waterstanden in zeeën en rivieren.* 1977.

34 J. Hemelrijk. *Oriënterende cursus mathematische statistiek.* 1977.

35 P.J.W. ten Hagen (red.). *Colloquium computer graphics.* 1978.

36 J.M. Aarts, J. de Vries. *Colloquium topologische dynamische systemen.* 1977.

37 J.C. van Vliet (red.). *Colloquium capita datastructuren.* 1978.

38.1 T.H. Koornwinder (ed.). *Representations of locally compact groups with applications, part I.* 1979.

38.2 T.H. Koornwinder (ed.). *Representations of locally compact groups with applications, part II.* 1979.

39 O.J. Vrieze, G.L. Wanrooy. *Colloquium stochastische spelen.* 1978.

40 J. van Tiel. *Convexe analyse.* 1979.

41 H.J.J. te Riele (ed.). *Colloquium numerical treatment of integral equations.* 1979.

42 J.C. van Vliet (red.). *Colloquium capita implementatie van programmeertalen.* 1980.

43 A.M. Cohen, H.A. Wilbrink. *Eindige groepen (een inleidende cursus).* 1980.

44 J.G. Verwer (ed.). *Colloquium numerical solution of partial differential equations.* 1980.

45 P. Klint (red.). *Colloquium hogere programmeertalen en computerarchitectuur.* 1980.

46.1 P.M.G. Apers (red.). *Colloquium databankorganisatie, deel 1.* 1981.

46.2 P.G.M. Apers (red.). *Colloquium databankorganisatie, deel 2.* 1981.

47.1 P.W. Hemker (ed.). *NUMAL, numerical procedures in ALGOL 60: general information and indices.* 1981.

47.2 P.W. Hemker (ed.). *NUMAL, numerical procedures in ALGOL 60, vol. 1: elementary procedures; vol. 2: algebraic evaluations.* 1981.

47.3 P.W. Hemker (ed.). *NUMAL, numerical procedures in ALGOL 60, vol. 3A: linear algebra, part I.* 1981.

47.4 P.W. Hemker (ed.). *NUMAL, numerical procedures in ALGOL 60, vol. 3B: linear algebra, part II.* 1981.

47.5 P.W. Hemker (ed.). *NUMAL, numerical procedures in ALGOL 60, vol. 4: analytical evaluations; vol. 5A: analytical problems, part I.* 1981.

47.6 P.W. Hemker (ed.). *NUMAL, numerical procedures in ALGOL 60, vol. 5B: analytical problems, part II.* 1981.

47.7 P.W. Hemker (ed.). *NUMAL, numerical procedures in ALGOL 60, vol. 6: special functions and constants; vol. 7: interpolation and approximation.* 1981.

48.1 P.M.B. Vitányi, J. van Leeuwen, P. van Emde Boas (red.). *Colloquium complexiteit en algoritmen, deel 1.* 1982.

48.2 P.M.B. Vitányi, J. van Leeuwen, P. van Emde Boas (red.). *Colloquium complexiteit en algoritmen, deel 2.* 1982.

49 T.H. Koornwinder (ed.). *The structure of real semisimple Lie groups.* 1982.

50 H. Nijmeijer. *Inleiding systeemtheorie.* 1982.

51 P.J. Hoogendoorn (red.). *Cursus cryptografie.* 1983.